An ESCRT grommet cooperates with a diffusion barrier to maintain nuclear integrity

Nicholas R. Ader[1], Linda Chen[1], Ivan V. Surovtsev[1,2], William L. Chadwick[1], Elisa C. Rodriguez[1], Megan C. King[1,3]*, and C. Patrick Lusk[1]*

[1] Department of Cell Biology, Yale School of Medicine, 295 Congress Ave, New Haven, CT, 06520

[2] Department of Physics, Yale University, New Haven, CT, 06511

[3] Department of Molecular, Cell and Developmental Biology, Yale University, New Haven, CT, 06511

* Correspondence: patrick.lusk@yale.edu, megan.king@yale.edu

ABSTRACT

The molecular mechanisms by which the endosomal sorting complexes required for transport (ESCRT) proteins contribute to the integrity of the nuclear envelope (NE) barrier are not fully defined. Here, we leveraged the single NE hole generated by mitotic extrusion of the *Schizosaccharomyces pombe* spindle pole body (SPB) to reveal two modes of ESCRT function executed by distinct complements of ESCRT-III proteins, both depending on CHMP7/Cmp7. A grommet-like function is required to restrict the NE hole in anaphase B, while replacement of Cmp7 by a sealing module ultimately closes the NE in interphase. Without Cmp7, nucleocytoplasmic compartmentalization surprisingly remains intact despite NE discontinuities up to 550 nm, suggesting mechanisms to prevent diffusion through these holes. We implicate SPB proteins as key components of a diffusion barrier acting with Cmp7 in anaphase B. Thus, NE remodeling mechanisms cooperate with proteinaceous diffusion barriers beyond nuclear pore complexes to protect the nuclear compartment.

INTRODUCTION

In eukaryotic cells, the genome is enclosed by the nuclear envelope (NE), which establishes a protected nuclear compartment. The NE is contiguous with the endoplasmic reticulum (ER) but is functionally specialized due to a unique proteome that populates its constituent inner, outer, and nuclear pore membranes. Nucleocytoplasmic compartmentalization relies on the integrity of these membranes and the selective barrier properties of nuclear pore complexes (NPCs) embedded in the NE (Dultz et al., 2022). During mitosis, the NE barrier presents a challenge for the spindle as it must access the duplicated chromosomes to faithfully segregate the genome to each daughter cell. Evolution has provided several solutions to this problem with a continuum of “closed” to “open” mitosis mechanisms employed in different organisms that reflects the degree to which the NE remains globally intact during chromosome segregation (Makarova and Oliferenko, 2016). In all scenarios, elaborate changes to the morphology of the NE during this period are universally observed, helping to ensure either the maintenance (in the case of a closed mitosis) or re-establishment (in the case of an open mitosis) of nucleocytoplasmic compartmentalization (Ungricht and Kutay, 2017).

These NE remodeling mechanisms are perhaps most elaborate at the end of the open mitosis of mammalian cells, when decondensing chromosomes are surrounded by nascent NE. Completion of NE sealing requires the closing of numerous NE fenestrations through an annular fusion mechanism thought to be executed by the endosomal sorting complexes required for transport (ESCRT) machinery, specifically the ESCRT-III proteins (Gu et al., 2017; Olmos et al., 2015; Olmos et al., 2016; Ventimiglia et al., 2018; Vietri et al., 2015; von Appen et al., 2020). A similar mechanism has been invoked in the sealing of nuclear pores housing defective NPCs (Thaller et al., 2019; Thaller et al., 2021; Webster et al., 2014; Webster et al., 2016) and at NE ruptures frequently observed in cancer cells or cells migrating through constrictions (Denais et al., 2016; Raab et al., 2016). While the events that underlie ESCRT-III mediated NE sealing have not been mechanistically delineated, parallels have been drawn with more extensively studied ESCRT-mediated membrane fission reactions. For example, during intralumenal vesicle (ILV) formation on endosomes, ESCRT-I/II recruit and activate the polymerization of ESCRT-III proteins (Vietri et al., 2020). ESCRT-III proteins can form single- and double-

63 stranded homo and heteropolymer filaments *in vitro*; such filaments have affinity for
64 negative or positive membrane curvature, perhaps influenced by the specific ESCRT-III
65 subunit composition (McCullough et al., 2018; Pfitzner et al., 2021; Remec Pavlin and
66 Hurley, 2020). The AAA+ ATPase VPS4 is required for the dynamic exchange of filament
67 subunits with a monomer pool (Adell *et al.*, 2017; Mierzwa et al., 2017) and for the ultimate
68 membrane fission step (McCullough *et al.*, 2018).

69 Despite the topological similarity between a NE hole and the neck of forming ILVs,
70 prior studies reveal distinct ESCRT requirements at the NE that hint at potentially unique
71 membrane remodeling and fission mechanisms. For example, ESCRT-I/II are
72 dispensable for the recruitment of ESCRT-III to the NE (Webster *et al.*, 2014). Further,
73 there is an ESCRT-II/III fusion protein, CHMP7 (Chm7 in *Saccharomyces cerevisiae* and
74 Cmp7 in *Schizosaccharomyces pombe/Schizosaccharomyces japonicus*), with a unique
75 function at the NE. Interestingly, unlike most ESCRT-mediated membrane remodeling
76 events that rely on peripheral membrane proteins, the recruitment of CHMP7 to the NE
77 requires a direct physical interaction with an integral inner nuclear membrane protein,
78 LEM2 (Heh1/Src1 in *S.c.* and Heh1/Lem2 in *S.p./S.j.*) (Gu *et al.*, 2017; Webster *et al.*,
79 2016). *In vitro* (von Appen *et al.*, 2020) and *in vivo* (Thaller *et al.*, 2019) evidence further
80 supports that LEM2 family members also activate CHMP7 polymerization. Moreover,
81 LEM2 and CHMP7 may form a membrane-embedded co-polymer that lines NE holes like
82 an O-ring, surrounding microtubules that remain attached to kinetochores (von Appen *et*
83 *al.*, 2020). Lastly, although ESCRT-III subunits including CHMP1A,B (Did2 in yeasts),
84 CHMP2A,B (Vps2 in *S.c.* and Did4 in *S.p./S.j.*), CHMP3 (Vps24 in yeasts), CHMP4A,B
85 (Snf7 in *S.c.* and Vps32 in *S.p/S.j.*), and IST1 (Ist1 in yeasts) have been shown to be
86 recruited to the NE alongside additional regulatory factors in metazoans including
87 CC2D1B (Ventimiglia *et al.*, 2018), Nesprin-2G (Wallis et al., 2021) and UFD1 (Olmos *et*
88 *al.*, 2015), we lack a quantitative spatiotemporal framework including the order, co-
89 dependency, and copy number of ESCRT proteins at a NE sealing site. This information
90 is critical to be able to fully elucidate how (and indeed whether) ESCRTs seal the NE and
91 will also lay the groundwork for further delineation of shared and unique mechanisms that
92 ESCRT proteins engage in to support a diverse range of membrane remodeling activities.

93 Despite clear evidence for recruitment of ESCRT proteins to the NE in late mitosis
94 (Gu *et al.*, 2017; Olmos *et al.*, 2015; Olmos *et al.*, 2016; Ventimiglia *et al.*, 2018; Vietri *et*
95 *al.*, 2015; von Appen *et al.*, 2020), several observations call into question whether the
96 ESCRT proteins are indeed necessary and/or sufficient to seal the NE. First,
97 compromising ESCRT by depletion of various subunits only delays, but does not
98 abrogate, the re-establishment of the accumulation of a soluble nuclear import reporter in
99 the nucleus after mitotic exit in human cells (Olmos *et al.*, 2015; Olmos *et al.*, 2016; von
100 Appen *et al.*, 2020) and the semi-open mitosis of *S. japonicus* (Lee et al., 2020; Pieper et
101 al., 2020). This result, which was mirrored by orthogonal studies modeling the repair of
102 interphase nuclear ruptures induced by laser ablation (Halfmann et al., 2019) or migration
103 through constrictions (Denais *et al.*, 2016; Raab *et al.*, 2016), suggest that there are
104 alternative, ESCRT-independent mechanisms by which nuclear compartmentalization is
105 reestablished. Indeed, Chm7/Cmp7 is dispensable for cell viability and global
106 nucleocytoplasmic compartmentalization in *S. cerevisiae* (Webster *et al.*, 2016) and *S.*
107 *pombe* (Dey et al., 2020; Gu *et al.*, 2017). One attractive explanation for these
108 observations is the existence of a redundant, ESCRT-independent NE sealing
109 mechanism(s). Indeed, genetic evidence in *Caenorhabditis elegans* and *S. japonicus*
110 suggests that altering phospholipid biosynthesis and/or membrane fluidity can mitigate
111 the ill effects of a compromised ESCRT-dependent NE sealing pathway (Lee *et al.*, 2020;
112 Penfield et al., 2020). Compensation by an orthogonal and CHMP7/Cmp7-independent
113 ESCRT-III sealing mechanism has also been proposed (Lee *et al.*, 2020). It is worth
114 considering, however, that most of these prior studies have relied on an indirect tool to
115 assess the integrity of the NE, namely the nuclear accumulation of a soluble reporter
116 containing a nuclear localization signal (NLS). Direct visualization of the continuity of the
117 NE membranes themselves, although more challenging, is ultimately essential to address
118 whether ESCRTs are necessary for NE sealing.
119 Here, we determine mechanisms of ESCRT function at the NE by taking
120 advantage of the fission yeast *S. pombe*. *S. pombe* inserts and extrudes its spindle pole
121 body (SPB) into and out of the NE at every mitotic entry and exit, respectively (Ding et
122 al., 1997). SPB extrusion thus leaves a single NE hole that must be sealed in each
123 daughter cell in a temporal and topological context similar, but much better defined than,

124 the numerous NE fenestrations present at the final stages of metazoan NE reformation.
125 We performed a comprehensive analysis of the complement, copy number, and relative
126 timing of ESCRT recruitment to the SPB extrusion site correlated to an ultrastructural
127 timeline of NE hole dynamics. In addition to providing definitive data that ESCRTs are
128 essential for ultimately sealing the NE, we also reveal an unexpected role for ESCRTs in
129 restricting the size of the NE hole during anaphase B in a manner akin to the function of
130 a grommet. Last, we uncover a mechanism that can explain the paradox of an apparently
131 intact nuclear compartment containing persistent NE holes: the existence of a
132 compensatory proteinaceous diffusion barrier that is sensitive to perturbation with 1,6
133 hexanediol and depends on components of the SPB, including pericentrin/Pcp1. Our
134 findings thus support both sealing dependent and independent functions for NE-recruited
135 ESCRTs while providing evidence for additional diffusion barriers beyond NPCs that
136 support the integrity of nucleocytoplasmic compartmentalization.
137

138 **RESULTS**

139 **ESCRTs are recruited in temporally distinct waves to the SPB extrusion site**

140 We hypothesized that Cmp7 and member(s) of the ESCRT-III family would be
141 recruited to the single NE hole generated in each fission yeast daughter cell nucleus upon
142 SPB extrusion during anaphase B (Ding *et al.*, 1997) (Figure 1A). We therefore tested the
143 localization of functional (see Methods) GFP-tagged ESCRT proteins, including: Cmp7,
144 Vps32, Ist1, Vps24, Did4, and Did2 (Figure 1B, Supplementary Figure S1A, and
145 Supplementary Table S1) in cells co-expressing Pcp1-mCherry or Sad1-mCherry as well
146 as mCherry-Atb2 (α-tubulin) to visualize the SPB and spindle microtubules, respectively
147 (Wälde and King, 2014). By relating spindle length (mCherry-Atb2 signal) to the rate of
148 anaphase B spindle elongation (Krüger et al., 2019), we categorized anaphase B cells as
149 early (0–5 min), mid (5–7.5 min), or late (>7.5 min).

150 We first determined the percentage of cells in each stage of the cell cycle where
151 individual GFP-ESCRTs co-localized with Pcp1-mCherry or Sad1-mCherry (Figures 1B
152 and 1C). Except for Cmp7-GFP, all GFP-ESCRTs localized to numerous cytoplasmic foci
153 that we interpret to be endosomes (Figure 1B). Consistent with the idea that ESCRTs are
154 only recruited to the NE when there is a NE hole, we rarely observed GFP-ESCRTs
155 colocalized with the SPB in G_2-phase of the cell cycle when the NE is expected to be fully
156 sealed (Figures 1B and 1C). In contrast, except for Did2-GFP, which was never seen at
157 the NE (Supplementary Figures S1A and S1B), all other tested ESCRT fusions
158 colocalized with the SPB marker in cells from mid anaphase B to late G_1/S phases
159 (Figures 1B and 1C), which correlates with the timing of SPB extrusion from the NE (Ding
160 *et al.*, 1997). Interestingly, the peak percentage of cells when a given GFP-ESCRT
161 accumulated at the SPB site could be temporally segregated into three waves: Cmp7
162 defined the first wave (Mid Ana B, “Wave 1”), Vps32 and Ist1 the second (Late Ana B,
163 “Wave 2”,), and Vps24 and Did4 the third (G_1/S, “Wave 3”) (Figure 1C).

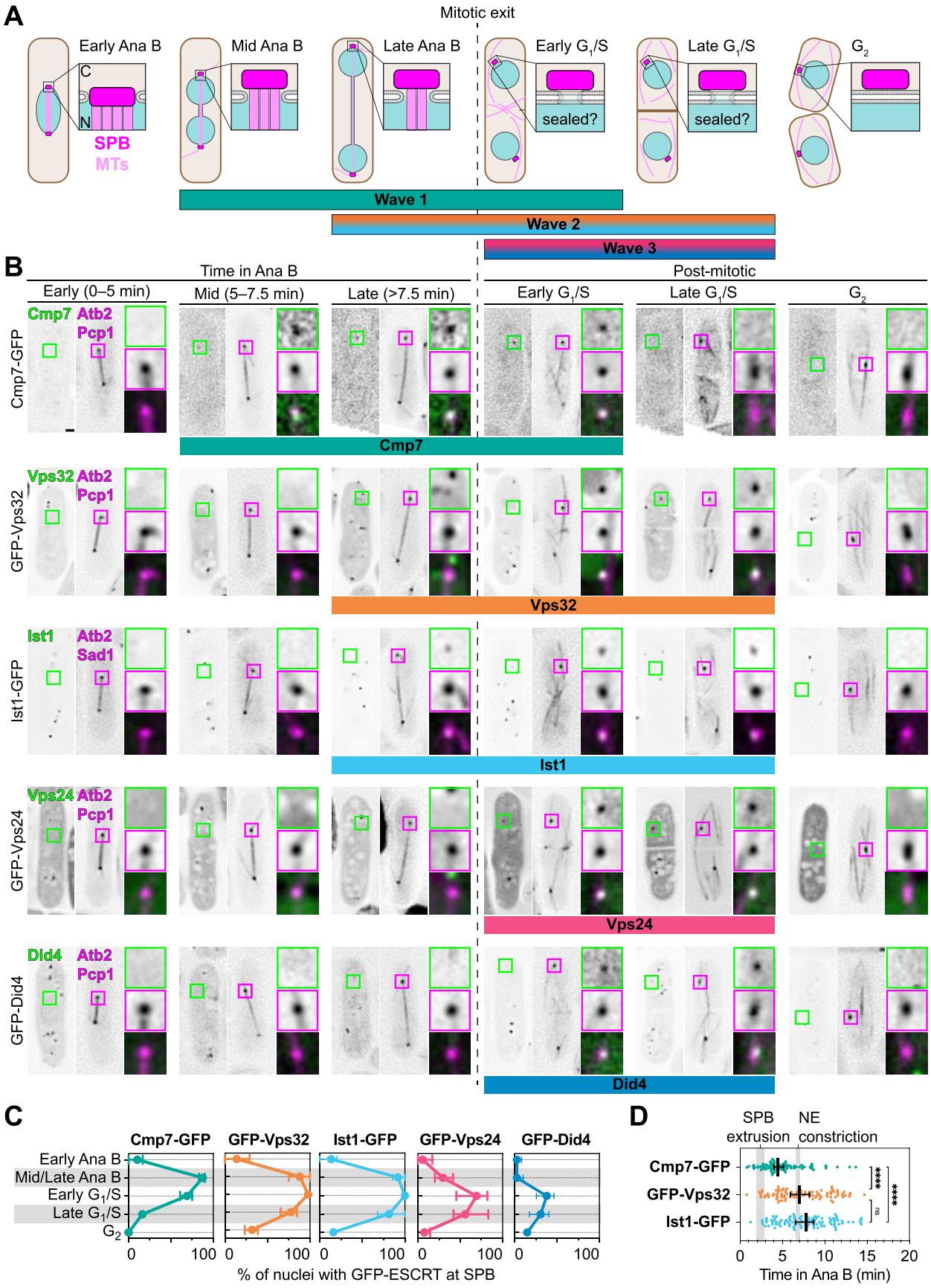
A
Mitotic exit
Early Ana B
Mid Ana B
Late Ana B
Early G1/S
Late G1/S
G2
C
N
SPB
MTs
sealed?
sealed?
Wave 1
Wave 2
Wave 3
B
Time in Ana B
Post-mitotic
Early (0–5 min)
Mid (5–7.5 min)
Late (>7.5 min)
Early G1/S
Late G1/S
G2
Cmp7-GFP
Cmp7 Atb2 Pcp1
Cmp7
GFP-Vps32
Vps32 Atb2 Pcp1
Vps32
Ist1-GFP
Ist1 Atb2 Sad1
Ist1
GFP-Vps24
Vps24 Atb2 Pcp1
Vps24
GFP-Did4
Did4 Atb2 Pcp1
Did4
C
Cmp7-GFP
GFP-Vps32
Ist1-GFP
GFP-Vps24
GFP-Did4
Early Ana B
Mid/Late Ana B
Early G1/S
Late G1/S
G2
0
100
% of nuclei with GFP-ESCRT at SPB
D
SPB extrusion
NE constriction
Cmp7-GFP
GFP-Vps32
Ist1-GFP
****
****
ns
0
5
10
15
20
Time in Ana B (min)

164

Figure 1. ESCRT proteins are recruited to the SPB extrusion site in three temporally distinct waves.

A: Diagrammatic representation of *S. pombe* cell cycle from early anaphase B through G_2 of the following cell cycle to establish the timeline in panel B. The spindle pole body (SPB) extrusion site from the nuclear envelope (NE) is magnified with the membrane architecture, if known, as described in Ding et al., 1997. N, nucleus (blue); C, cytoplasm (beige); SPB, dark magenta; microtubules (MTs), light magenta. Duration of the three waves of ESCRT recruitment observed in this study are indicated by labeled colored bars. Mitotic exit is indicated by the dotted vertical line.

B: Gallery of live-cell fluorescence micrographs of GFP-tagged ESCRT proteins in *S. pombe* representative of cell populations at the indicated cell cycle stages (see key in A). In each subpanel, images of the GFP-ESCRT are on left, sum projection (over 4.8 µm) of mCherry-Atb2/Pcp1-mCherry or mCherry-Atb2/Sad1-mCherry in middle and magnifications of square region of interest (ROI) shown vertically arranged at right with (top to bottom) green, magenta and merged channels. To maximize image clarity, fluorescence intensity of magnified ROIs were independently adjusted in the linear range with the exception of the magenta channel where the gamma was adjusted to 0.05 to allow visualization of mCherry-Atb2 and Pcp1-mCherry or Sad1-mCherry without saturation. Colored bars below images indicate timing of peak ESCRT recruitment in the population (see C). Scale bar, 1 µm. Magnified ROIs, 1.6 µm wide. Cmp7-GFP, MKSP3363; GFP-Vps32, MKSP3353; Ist1-GFP, MKSP3365; GFP-Vps24, MKSP3352; GFP-Did4, MKSP3334.

C: Plots of the percentage of nuclei with indicated GFP-ESCRT colocalized with SPB marker at indicated phases of the cell cycle. Points and error bars represent mean and range, respectively, across at least three biological replicates with at least 50 nuclei/GFP-ESCRT/replicate. Cmp7-GFP (MKSP3363), N = 408 nuclei; GFP-Vps32 (MKSP3353), N = 442 nuclei; Ist1-GFP (MKSP3365), N = 401 nuclei; GFP-Vps24 (MKSP3352), N = 699 nuclei; GFP-Did4 (MKSP3334), N = 623 nuclei.

D: Scatter plot where each data point represents the time in anaphase B that a GFP-ESCRT was first visible colocalized with the SPB marker across three biological replicates. Bar and error bars represent mean and standard deviation of points, respectively. Vertical gray bars indicate one standard deviation of the mean across three biological replicates for Cut11-GFP (MKSP1697) focal loss (SPB extrusion, 1.96–2.87 min) and NE constriction (6.59–7.06 min) (N = 75 cells (25 cells/replicate)). Kruskal-Wallis test performed across all datasets with Dunn's multiple comparisons across all datasets (****, $p < 0.001$; n=100; at least 17 nuclei/strain/replicate).

To further probe the relative timing of Wave 1 and Wave 2, we performed timelapse microscopy of cells progressing through mitosis expressing Cmp7-GFP, GFP-Vps32, or Ist1-GFP. We plotted the timing of the arrival (i.e., the first frame when observed) of each GFP-ESCRT at the SPB extrusion site with respect to anaphase B progression (Figure 1D). We also placed this timeline in the context of the loss of Cut11 at the SPB, which is thought to reflect SPB extrusion, and nuclear constriction into a dumbbell shape (Figure 1D, vertical grey bars) (West et al., 1998). Using this approach, we confirmed that Cmp7-GFP was recruited to the SPB site significantly earlier than GFP-Vps32 and Ist1-GFP, which were detected with similar timing (Figure 1D). Finally, to rigorously test if we could temporally segregate the Wave 1 and 2 ESCRTs in anaphase, we examined the localization of Cmp7-GFP and Ist1-mCherry within the same cell. Indeed, we found that Cmp7-GFP appeared at the SPB extrusion site prior to recruitment of Ist1-mCherry (Supplementary Figure S1C). Thus, taken together, we conclude that

178 there are three temporally distinct waves of ESCRT-III recruitment to the SPB extrusion
179 site: (1) Cmp7 in mid anaphase B, (2) Vps32/Ist1 in late anaphase B, and (3) Vsp24/Did4
180 in the subsequent G_1/S when Cmp7 departs (Figure 1A).
181
182 **ESCRT protein copy number at the SPB extrusion site**
183 With perhaps one exception (Adell *et al.*, 2017), there remains uncertainty
184 regarding the range of numbers of ESCRT subunits required to execute a given
185 membrane fission reaction. Therefore, to inform on the organization and architecture of
186 the ESCRT polymers at the fission yeast NE, we calculated ESCRT subunit copy number
187 at the SPB extrusion site using a semi-automated ratiometric fluorescence quantification
188 approach. We directly related GFP-ESCRT fluorescence at the SPB site to kinetochore
189 foci formed by a GFP-tagged kinetochore protein, Fta3, which is found at ~37 molecules
190 per kinetochore (for details see Methods and Supplementary Figures S2A–S2C)
191 (Lawrimore *et al.*, 2011).
192 Using the Fta3-GFP foci as standards, we quantified the average copy number of
193 all ESCRT subunits recruited to the SPB extrusion site in anaphase B and G_1/S (Table
194 1). Overall, there was an average of 16 ± 8 molecules of Cmp7-GFP per SPB extrusion
195 site. The spread in the Cmp7-GFP numbers did not reflect any change in copy number
196 during anaphase B progression or into the subsequent G_1/S-phases (Supplementary
197 Figures S2D and S2E). The Wave 2 ESCRT GFP-Vps32, regardless of mitotic stage, was
198 found at a much higher copy number of 72 ± 41 molecules (Supplementary Figures S2D
199 and S2F), suggesting an approximate 1 to 5 stoichiometry of Cmp7 to Vps32 molecules
200 at this NE hole. The Wave 3 ESCRT subunits GFP-Vps24 and GFP-Did4 were calculated
201 to be 77 ± 51 and 25 ± 10 molecules/focus, respectively (Supplementary Figure S2D).
202 The one exception to an apparently stochastic variation in ESCRT subunit copy number
203 was the Wave 2 protein Ist1-GFP, which increased in number from 25 ± 13 molecules in
204 anaphase B to 34 ± 18 into G_1/S (Supplementary Figure S2D). Consistent with an
205 increase in Ist1 copy number through anaphase B, there was a positive correlation
206 between Ist1-GFP copy number at individual NE holes with anaphase B progression

Protein	Mitotic NE hole						ILV Formation[1]
	Ana B		G_1/S		All		
	Mean ± SD	N	Mean ± SD	N	Mean ± SD	N	Mean
Cmp7	16 ± 8	88	15 ± 8	108	15 ± 8	196	*n.r.*
Vps32	75 ± 45	33	69 ± 37	35	72 ± 41	68	75–200
Ist1	25 ± 13	67	34 ± 18	80	30 ± 17	147	*n.m.*
Vps24	*n.m.*		77 ± 51	24	77 ± 51	24	15–50
Did4	*n.r.*		25 ± 10	26	25 ± 10	26	*n.m*

Table 1. Average copy number for ESCRT proteins at the NE. Copy number is shown for all examined ESCRTs by cell cycle. Copy number at intralumenal vesicle (ILV) formation at endosomes as reported in Adell et al. (2017). *n.r.,* not recruited. *n.m.,* not measured.

207 (Supplementary Figure S2G). This incremental accumulation of an ESCRT was not
208 observed for other ESCRTs in our work or that of others at ILVs (Adell *et al.*, 2017),
209 suggesting that it could be a behavior unique to Ist1.
210
211 **Cmp7 is required for ESCRT recruitment to the NE**
212 The sequential timing of ESCRT recruitment waves to the NE suggests a
213 dependency of the later wave ESCRTs on those preceding them. To test this idea, we
214 next determined the co-dependency of ESCRT protein recruitment to the mitotic NE hole.
215 As predicted from prior work in budding yeast (Webster *et al.*, 2016) and cultured human
216 cells (Gu *et al.*, 2017), the recruitment of Cmp7-GFP to the SPB site required Heh1/Lem2
217 but not its paralog Heh2/Man1 (Figures 2A and 2B). Consistent with the observed
218 sequential nature of ESCRT recruitment, Wave 2 or 3 ESCRTs failed to be recruited to
219 the NE in the absence of the Wave 1 Cmp7 (Figure 2C). Thus, as has been observed in
220 other contexts (Gu *et al.*, 2017; Olmos *et al.*, 2016; Thaller *et al.*, 2019; Vietri *et al.*, 2015),
221 Cmp7 is required for all ESCRT-III recruitment to the NE.
222 We next tested the requirement of Wave 2 ESCRTs for recruitment of other GFP-
223 ESCRTs. As shown in Figure 2D, Ist1 is entirely dispensable for all GFP-ESCRT
224 recruitment to the SPB extrusion site. Interestingly, Ist1-GFP recruitment is compromised
225 but not completely abrogated in the absence of its Wave 2 partner, Vps32, appearing
226 both later and in a smaller percentage of cells compared to WT (Figure 2E). Thus,

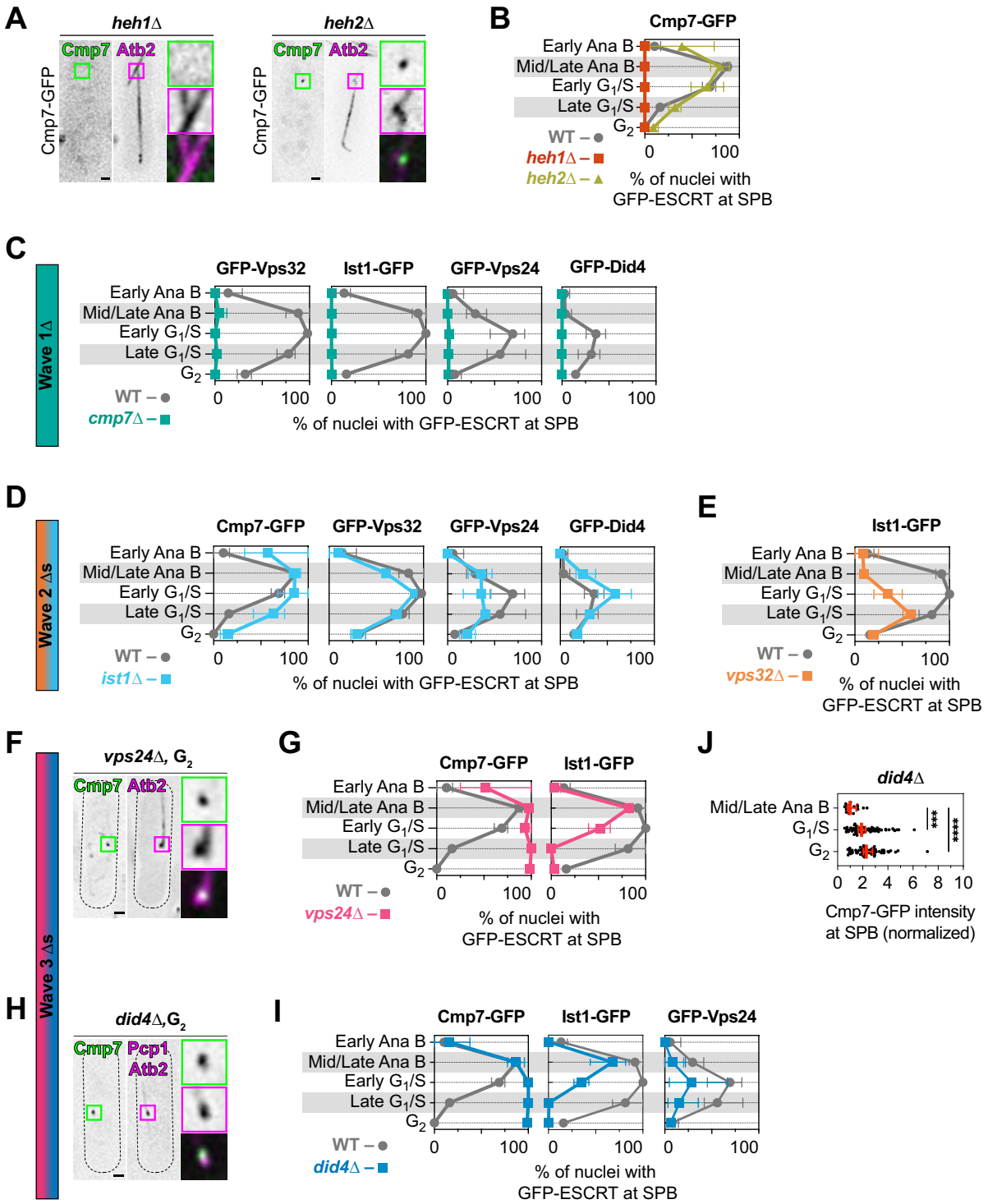

Figure 2. Cmp7 is required for ESCRT-III recruitment to the NE and is replaced by Wave 3 ESCRTs.
Figure legend continued next page.

227 although Cmp7 is essential for any ESCRT-III subunit recruitment, there may not be a
228 strict assembly order for other downstream filament assembly events.

Figure 2. Cmp7 is required for ESCRT-III recruitment to the NE and is replaced by Wave 3 ESCRTs.

A: Fluorescence micrographs of Cmp7-GFP and mCherry-Atb2 in representative *heh1*Δ (left) and *heh2*Δ (right) cells in anaphase B. In each subpanel, images of the Cmp7-GFP are on the left, sum projection (over 4.8 µm) of mCherry-Atb2 in middle and magnifications of square ROI shown vertically arranged at right with (top to bottom) green, magenta and merged channels. Fluorescence intensity of magnified ROIs were independently adjusted in the linear range. Scale bar, 1 µm. Magnified ROIs, 1.6 µm wide.

B: Plots of the percentage of nuclei with Cmp7-GFP foci colocalized with the SPB site in WT (gray circles), *heh1*Δ (red squares), and *heh2*Δ (yellow triangles) strains in indicated phases of the cell cycle. Points and error bars represent mean and range, respectively, across at least three biological replicates with at least 50 nuclei/Cmp7-GFP/replicate. Cmp7-GFP, WT (data from Figure 1C), Cmp7-GFP, *heh1*Δ (MKSP3259), N = 203; Cmp7-GFP, *heh2*Δ (MKSP3275), N = 275 nuclei.

C: As in B but with the indicated GFP-ESCRTs in WT (gray circles) or *cmp7*Δ (green squares) cells. Points and error bars represent mean and range, respectively, across at least three biological replicates with at least 50 nuclei/GFP-ESCRT/replicate. All WT data from Figure 1C; GFP-Vps32, *cmp7*Δ (MKSP3354), N = 628 nuclei; Ist1-GFP, *cmp7*Δ (MKSP3447), N = 384 nuclei; GFP-Vps24, *cmp7*Δ (MKSP3355), N = 702 nuclei; GFP-Did4, *cmp7*Δ (MKSP3366), N = 372 nuclei.

D: As in B but with the indicated GFP-ESCRTs in WT (gray circles) or *ist1*Δ (blue squares) cells. Points and error bars represent mean and range, respectively, across at least three biological replicates with at least 50 nuclei/GFP-ESCRT/replicate. All WT data from Figure 1C; Cmp7-GFP, *ist1*Δ (MKSP3429), N = 418 nuclei; GFP-Vps32, *ist1*Δ (MKSP3449), N = 550 nuclei; GFP-Vps24, *ist1*Δ (MKSP3669), N = 323 nuclei; GFP-Did4, *ist1*Δ (MKSP3668), N = 455 nuclei.

E: As in B but with Ist1-GFP in WT (gray circles) or *vps32*Δ (orange squares) cells. Ist1-GFP, WT (data from Figure 1C), Ist1-GFP, *vps32*Δ (MKSP3504), N = 382 nuclei.

F: As in A but in *vps24*Δ, G_2 cells.

G: As in B but with the indicated GFP-ESCRTs in WT (gray circles) or *vps24*Δ (red squares) cells. All WT data from Figure 1C; Cmp7-GFP, *vps24*Δ (MKSP3387), N = 236 nuclei; Ist1-GFP, *vps24*Δ (MKSP3544), N = 378 nuclei.

H: As in A but in *did4*Δ, G_2 cells. Gamma was adjusted to 0.05 to allow visualization of mCherry-Atb2 and Pcp1-mCherry without saturation.

I: As in B but with the indicated GFP-ESCRTs in WT (gray circles) or *did4*Δ (blue squares) cells. All WT data from Figure 1C; Cmp7-GFP, *did4*Δ (MKSP3381), N = 323 nuclei; Ist1-GFP, *did4*Δ (MKSP3496), N = 376 nuclei; GFP-Vps24, *did4*Δ (MKSP3511), N = 438 nuclei.

J: Plot of the fluorescence intensity of Cmp7-GFP at the SPB site in *did4*Δ cells (MKSP3381) at indicated cell cycle stages normalized to median mid/late anaphase B value for each biological replicate. Bar and error bars represent mean and standard deviation of points, respectively. Kruskal-Wallis test performed across all datasets with Dunn's multiple comparisons across all dataset (****, $p < 0.001$; N=160, at least 45 cells/replicate).

229

230 **Cmp7 is replaced by Wave 3 ESCRT assemblies in G_1/S**

231 As our temporal analysis suggests progressive remodeling of the ESCRT
232 complement at the NE hole in concert with the cell cycle, we next tested whether the
233 inability to recruit the final wave of ESCRTs impacted the dynamics of the upstream Wave
234 1 or 2 ESCRTs. Strikingly, even though the Wave 3 ESCRTs Vps24 and Did4 were found
235 at the SPB site when the majority of Cmp7 had departed in most WT cells (Figure 1), we
236 found that Cmp7-GFP recruitment was dysregulated in *vps24*Δ and *did4*Δ cells, remaining
237 at the NE throughout G_1/S and even G_2 (Figures 2F–2I). Moreover, Cmp7-GFP over-

238 accumulated at the NE in *vps24*Δ and *did4*Δ cells with a median 2-fold greater
239 fluorescence than in WT cells (Figure 2J). Interestingly, although the initial recruitment of
240 the Wave 2 ESCRT Ist1-GFP was normal in *vps24*Δ and *did4*Δ cells, Ist1-GFP failed to
241 persist with the same kinetics observed in WT cells (Figures 2G and 2I). Moreover,
242 although still observed in a small percentage of SPB extrusion sites, Vps24 recruitment
243 was largely dependent on its Wave 3 partner, Did4 (Figure 2I). Thus, we interpret these
244 data in a model in which the inability to complete ESCRT remodeling during G_1/S drives
245 a reversal of the ESCRT order into an aberrant Wave 1 state with persistent Cmp7-GFP
246 recruitment.
247
248 **ESCRT waves correlate to changes in NE hole morphology**
249 To help understand ESCRT function from anaphase to G_1/S, we correlated the
250 ESCRT recruitment timeline to the ultrastructure of the NE hole at the SPB extrusion site
251 using correlative light and electron microscopy (CLEM) and electron tomography (Figure
252 3). We used Pcp1-mCherry and Cdc7-GFP, the latter of which transiently localizes to
253 mitotic/G_1 spindle poles (Sohrmann et al., 1998), to help inform the location of the SPB
254 extrusion site and the cell cycle stage of embedded cells. At the correlated location of
255 these SPB markers, we identified the SPB plaque as an electron-dense region in the
256 cytoplasm apposing the nucleus (Figures 3A–3D, red outline). We also observed an
257 electron-lucent region of cytosol surrounding the SPB plaques that excluded ribosomes
258 (Figures 3A–D, orange outline).
259 The onset of Wave 1 ESCRT recruitment occurs in mid anaphase B; in early/mid
260 anaphase B cells examined (n=10) we observe a median value of the fenestration the NE
261 apposing the SPB of 140 nm (Figure 3A, black arrowhead; Figure 3I); spindle
262 microtubules passed through this hole in select virtual slices of the entire tomogram
263 (Movie 1). Interestingly, we observed a narrowing of the NE hole to a median of 59 nm in
264 late anaphase B cells, alongside a reduction of microtubule number (Figure 3B, black
265 arrowhead; Figure 3I, n=5) (Movie 2) (Ding *et al.*, 1997). These data suggest that the
266 recruitment of the Wave 2 ESCRTs temporally correlates with a constriction of the NE
267 hole from ~140 to ~60 nm. Subsequently, in G_1/S cells there was either a relaxation of
268 the NE hole to a median of 184 nm (n=4; Figure 3C, black arrowhead and 3I)

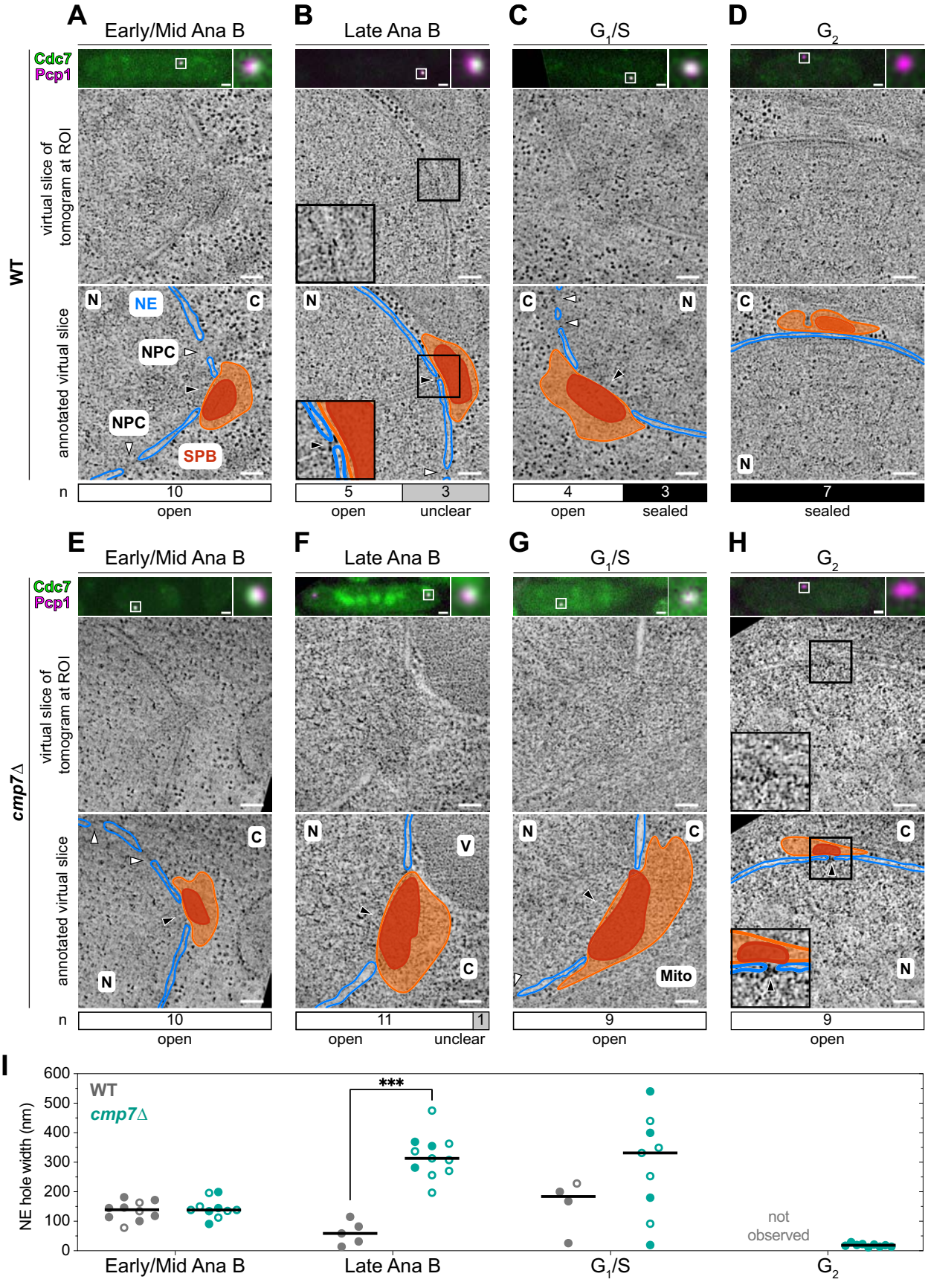
A
Early/Mid Ana B
B
Late Ana B
C
G1/S
D
G2
Cdc7
Pcp1
WT
virtual slice of tomogram at ROI
annotated virtual slice
N
NE
C
NPC
NPC
SPB
n
10
open
5
3
open
unclear
4
3
open
sealed
7
sealed
E
Early/Mid Ana B
F
Late Ana B
G
G1/S
H
G2
cmp7Δ
V
Mito
11
1
9
9
I
NE hole width (nm)
WT
cmp7Δ
***
not observed
Early/Mid Ana B
Late Ana B
G1/S
G2

269

Figure 3. Cmp7 is required to restrict the size of the NE hole in anaphase and seal the NE in G_1/S.

A–D: Top, fluorescence micrograph of a thick section of a resin-embedded yeast strain (MKSP3180) expressing Cdc7-GFP (green) and Pcp1-mCherry (magenta) prepared for correlative light and electron microscopy (CLEM) and electron tomography (ET). The indicated cell cycle stages were determined by a combination of fluorescence marker presence/localization and ultrastructural features. The white square in the fluorescence micrographs indicates regions where the electron tomogram was collected and is shown magnified at the right. Middle and bottom panels are a virtual slice taken from the electron tomogram shown without (middle) and with (bottom) manual annotation of features. NE, blue, SPB plaques, red, electron-lucent ribosome exclusion zone extending beyond SPB plaques, orange. White arrowheads, NPC. Black arrowheads, SPB extrusion hole. N, nucleus; C, cytoplasm. Scale bars: fluorescence micrographs, 1 µm; virtual slices from electron tomogram, 100 nm.

E–H: CLEM and ET for *cmp7*Δ cells (MKSP3243), prepared and displayed as in A. Mito, mitochondria; V, vacuole.

I: Scatter plot of NE hole widths in tomograms of WT (gray circles) and *cmp7*Δ (green circles). Solid circles represent exactly determined diameters while open circles represent minimum values in cases where the full diameter was not visualized in the volume. Black bars represent median. Mann-Whitney test performed between WT and *cmp7*Δ for each cell cycle phase individually (***, $p < 0.0001$; all others, $p \geq 0.05$). WT cells, MKSP3180, N = 14 nuclei; *cmp7*Δ cells, MKSP3243, N = 39 nuclei.

or cells that had completed NE sealing (n=3), suggesting that the timing of Wave 3 corresponds to the act of NE sealing. Consistent with this interpretation, the NE membranes were continuous in all 7 G_2-phase cells examined (Figures 3D and 3I). Thus, each wave of ESCRT recruitment corresponds to distinct morphological changes of the NE hole; Wave 2 corresponds to a transient NE constriction while Wave 3 represents a timepoint that is suggestive of a role in NE sealing.

ESCRTs restrict the size of the NE hole during mitosis

To directly evaluate whether ESCRTs impact the observed NE hole dynamics, we performed CLEM on *cmp7*Δ cells, which fail to recruit all ESCRT-III proteins (Figure 2C). Loss of *CMP7* did not impact the morphology of the NE fenestration in early/mid anaphase B cells, which were similar to those in WT cells (n=10; Figures 3E and 3I; Movie 3). In striking contrast, late anaphase B *cmp7*Δ cells (n=12) exhibited massive NE gaps with a median width of 313 nm and a high variation (range of 197–475 nm; Figures 3F and 3I; Movie 4), an approximate five-fold increase compared to WT cells at the same stage. Thus, we conclude that Cmp7 is required to restrict the diameter of the mitotic NE hole during anaphase B. Given that this state temporally precedes the recruitment of Wave 3 ESCRTs (Figure 1), this function is likely carried out by Wave 1 and Wave 2 ESCRTs.

289 **Cmp7 is required but must be remodeled to Wave 3 ESCRTs to promote NE sealing**

290 Interestingly, in G_1/S when some WT NE holes had been sealed, NE gaps that
291 ranged from 20 to 540 nm (median, 332 nm) were observed in all imaged *cmp7*Δ cells;
292 n=6, Figures 3G and 3I). Although not statistically different, the large spread of values in
293 individual *cmp7*Δ cells suggests that the aberrantly large fenestrations arising in
294 anaphase B persist into the subsequent G_1/S. Most strikingly, G_2 *cmp7*Δ cells (n=9, Figure
295 3H) retained a discernable but small median 19 nm NE fenestration (Figure 3I),
296 suggesting that an ESCRT-independent mechanism ultimately constricted, but failed to
297 seal, the NE.

298 As our light microscopy data indicated that Cmp7 aberrantly persists in cells
299 lacking Wave 3 ESCRTs (Figures 2F–2J), we also interrogated the morphological
300 consequences of reversion to an aberrant Wave 1 assembly state by applying CLEM and
301 electron tomography to G_2 *did4*Δ cells (Figures 4A and 4B). At the majority (8/13) of
302 Cmp7-GFP NE foci we selected, we correlated the fluorescence to a median 21 nm hole
303 in the NE (Figure 4C), suggesting that the persistent Wave 1 state also disrupts NE
304 sealing; in the other 5 samples, we could not unambiguously observe a NE hole (Figures
305 4A and 4B). Unlike in *cmp7*Δ cells, however, in *did4*Δ cells we found that the persistent
306 NE hole was filled with densely stained material (Figure 4A), which we interpret to be
307 Cmp7-GFP, although other, yet to be defined factors may also be present. Interestingly,
308 although Cmp7-GFP persisted at the SPB extrusion site throughout G_2 in *did4*Δ cells, it
309 disappeared with the onset of the subsequent SPB insertion cycle (Figure 4D). These
310 data suggest a mechanism to "reset" the SPB site for another round of SPB insertion,
311 extrusion and NE sealing that might entail clearing aberrant ESCRT assemblies from the
312 NE. Thus, we conclude that Cmp7's role in initiating ESCRT-III assembly is required to
313 close the constricted, 20 nm NE fenestration in G_2. Moreover, the loss of Wave 3 ESCRTs
314 leads to the accumulation of Cmp7 in NE holes that fail to seal, highlighting that it is the
315 replacement of the initial Wave 1/Wave 2 ESCRT assemblies to the Wave 3 ESCRT state
316 that ultimately drives the sealing reaction.
317

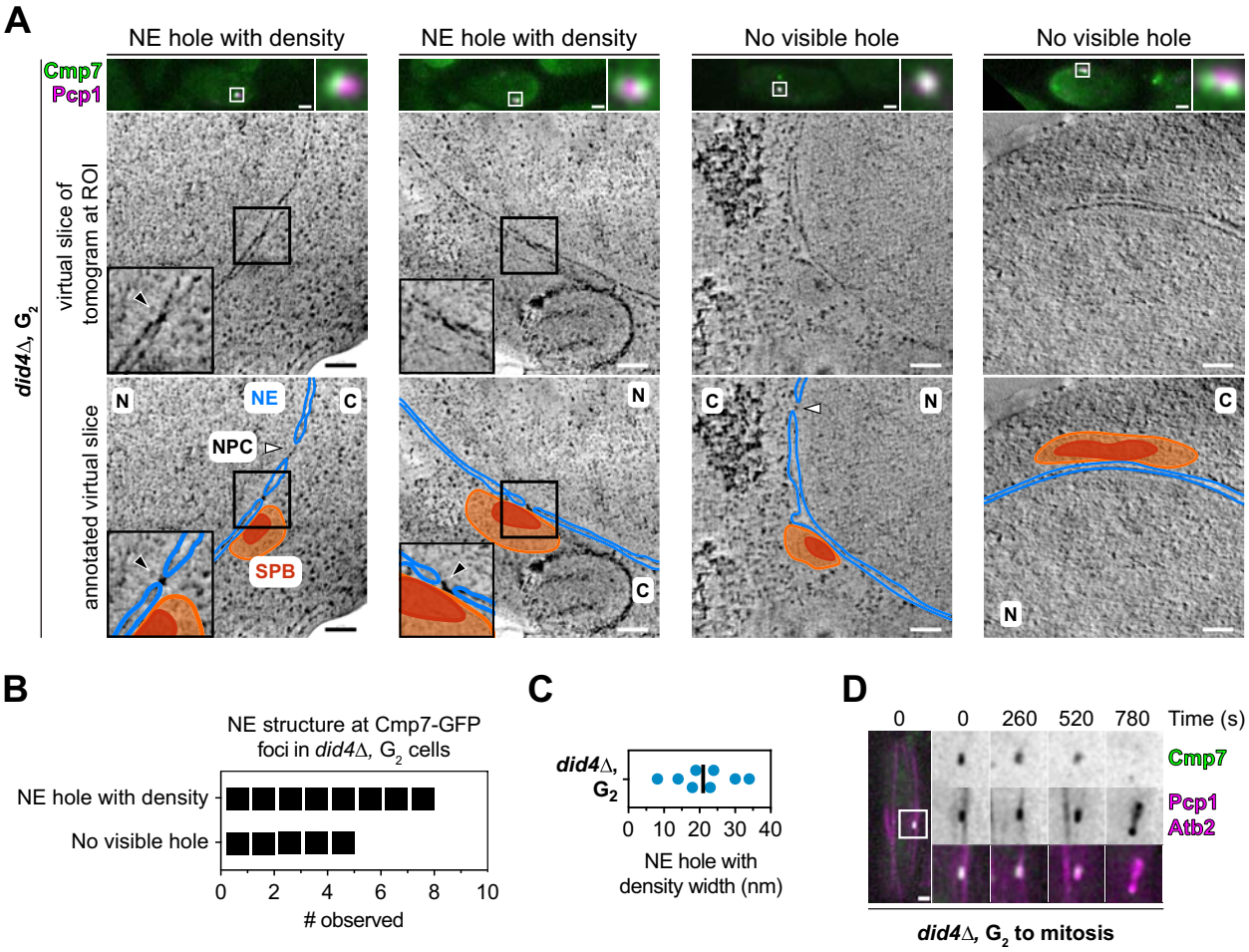

318

Figure 4. Did4 is required to remove Cmp7 to seal the NE.

A: Gallery of four representative electron tomograms showing either NE holes filled with electron density (left) or no visible NE holes (right). In each sub panel: Top, fluorescence micrograph of a thick section of a resin-embedded *did4*Δ strain (MKSP3381) in G_2 expressing Cmp7-GFP (green) and Pcp1-mCherry (magenta) prepared for CLEM and ET. The white square in the fluorescence micrographs indicates the region where the electron tomogram was collected and is shown magnified at right. Middle and bottom panels are a virtual slice taken from the electron tomogram shown without (middle) and with (bottom) manual annotation of features. NE, blue, SPB plaques, red, electron-lucent ribosome exclusion zone extending beyond SPB plaques, orange. White arrowheads, NPC. Black arrowheads, NE hole with density. N, nucleus; C, cytoplasm. Scale bars: fluorescence micrographs, 1 µm; virtual slices from electron tomogram, 100 nm.

B: Plot of the number of occurrences (black squares) of the observed NE phenotypes from A. MKSP3381, N = 13 nuclei.

C: Scatter plot of NE hole widths (nm) observed in *did4*Δ, G_2 cell tomograms as in A. Black bar represents median. MKSP3381, N = 8 nuclei.

D: Fluorescence micrographs of a timelapse series (top, seconds representing the transition from G_2 into mitosis) of a *did4*Δ cell expressing Cmp7-GFP (green), Pcp1-mCherry (magenta), and mCherry-Atb2 (magenta). The white square in the overview micrograph indicates the ROI magnified in the image series vertically arranged at right with (top to bottom) green, magenta and merged channels. Representative cell (MKSP3381) from three biological replicates of imaging N = 180 cells, at least 60 cells/replicate.

319 **Cmp7 is dispensable for maintaining nucleocytoplasmic compartmentalization**

320 The persistence of NE holes at the SPB extrusion site throughout the cell cycle in
321 *cmp7*Δ cells, and in particular the massive NE fenestrations observed during mitosis,
322 prompted an evaluation of nucleocytoplasmic compartmentalization in these conditions.
323 As the steady-state distribution of NLS-containing reporters, and by inference NPC
324 function, are not affected by the loss of *CMP7* (Gu *et al.*, 2017), we investigated the
325 passive nuclear exclusion of large reporters lacking nuclear import or export signals.
326 Specifically, we tested the distribution of GFP fused to either three (MGM2) or five
327 (MGM4) maltose-binding proteins; while MGM2 is able to diffuse across NPCs, the larger
328 MGM4 construct is effectively excluded from the nucleus (Figure 5A and Supplementary
329 Figure S3A) (Popken et al., 2015). Consistent with this, most MGM2 cells had nuclear to
330 cytoplasmic ratios (N/C ratios) >0.75 and most MGM4 cells had N/C ratios <0.75; we
331 therefore used N/C ratio = 0.75 as a cut-off to gauge whether cells expressing MGM4
332 displayed a defect in their nucleocytoplasmic compartmentalization (Supplementary
333 Figure S3A). Using this framework, we found that *cmp7*Δ cells displayed no detectable
334 loss of nuclear compartmentalization (Figure 5A).

335

336 **Cmp7 cooperates with a diffusion barrier to maintain the nuclear compartment**

337 The observation that deletion of *CMP7* did not appreciably impact
338 nucleocytoplasmic compartmentalization despite the presence of large NE fenestrations
339 was, on the surface, surprising. It should be considered, however, that even in WT cells
340 there is a period (~14 minutes) after SPB extrusion when the nuclear compartment
341 appears intact despite the presence of a NE fenestration of at least ~60 nm but up to 228
342 nm beneath the SPB (Figure 3). Thus, there must be additional, unidentified diffusion
343 barrier(s) (beyond the NPC) capable of maintaining nucleocytoplasmic
344 compartmentalization in the face of a persistent NE hole. To begin to test this idea, we
345 employed 1,6-hexanediol (1,6-HD), an aliphatic alcohol that disrupts weak hydrophobic
346 protein-protein interactions including that of FG-repeat containing nucleoporins that
347 contribute to the NPC diffusion barrier (Ribbeck and Görlich, 2002; Riquelme Barrientos
348 et al., 2023; Shulga and Goldfarb, 2003). We observed that 5%, but not 2.5%, 1,6-HD

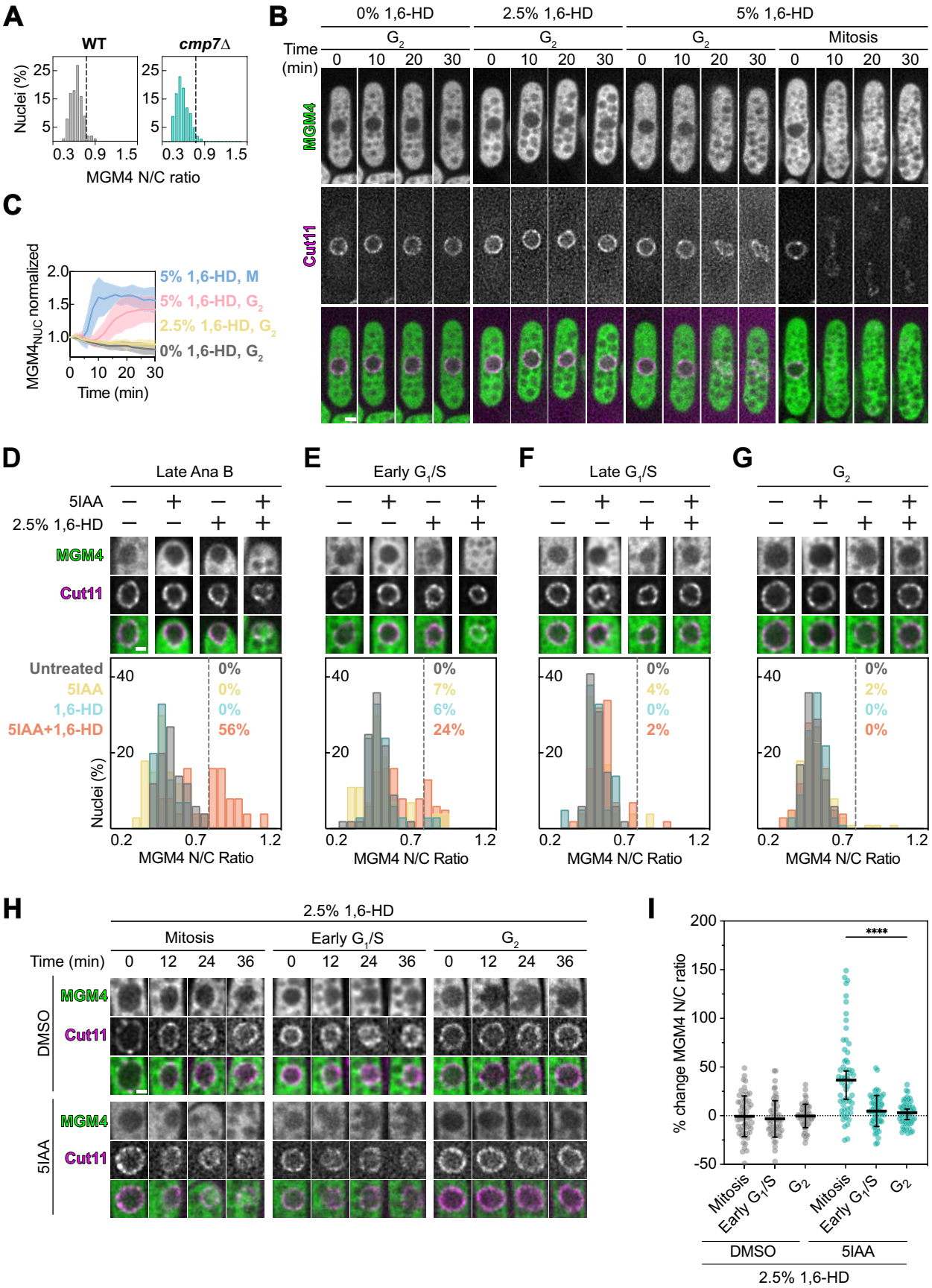
A
WT
cmp7Δ
Nuclei (%)
MGM4 N/C ratio
B
0% 1,6-HD
2.5% 1,6-HD
5% 1,6-HD
Time (min)
MGM4
Cut11
C
MGM4NUC normalized
5% 1,6-HD, M
5% 1,6-HD, G2
2.5% 1,6-HD, G2
0% 1,6-HD, G2
Time (min)
D
Late Ana B
E
Early G1/S
F
Late G1/S
G
G2
5IAA
2.5% 1,6-HD
Untreated
5IAA
1,6-HD
5IAA+1,6-HD
Nuclei (%)
MGM4 N/C Ratio
H
2.5% 1,6-HD
Mitosis
Early G1/S
G2
Time (min)
DMSO
5IAA
I
% change MGM4 N/C ratio
****
Mitosis
Early G1/S
G2
DMSO
5IAA
2.5% 1,6-HD

349

Figure 5. Cmp7 and a 1,6 hexanediol-sensitive diffusion barrier ensure nucleocytoplasmic compartmentalization during mitosis.

A: Histogram relating nucleoplasmic and cytoplasmic GFP fluorescence of MGM4 in a N/C ratio of individual WT and *cmp7*Δ cells across three biological replicates. Size between bins, 0.05. Dotted line at 0.75 bin. WT (MKSP3345 and MKSP3488), N = 240 nuclei; *cmp7*Δ (MKSP3535), N= 177 nuclei.

B: A time-lapse series of deconvolved fluorescence micrographs of cells (MKSP3699) expressing MGM4 and Cut11-mCherry. MGM4 (green, top), Cut11-mCherry (magenta, middle) and merged image (bottom) shown. Cells were treated with 0%, 2.5% or 5% 1,6-hexanediol (1,6-HD) as indicated. For G_2 cells, time 0 indicates the start of imaging after the delivery of 1,6-HD by microfluidics. For mitotic cells, only cells that went through mitosis after 1,6-HD treatment were considered. Across the population, the constriction of the NE into a dumbbell shape (~10 min) was used to align individual traces in C. Scale bar, 1 µm. Representative of 20 cells per condition with at least 5 cells per condition for each of three biological replicates.

C: Plot of the nuclear (NUC) fluorescence of MGM4 through timelapse imaging experiments as shown in B normalized to the initial timepoint for each individual nucleus of a cell (MKSP3699, untreated). Solid lines represent average of 20 cells per condition with at least 5 cells per condition for each of three biological replicates, with the shaded region representing the standard deviation. M = mitosis.

D–G: Asynchronous cells (MKSP3699) expressing MGM4, Cut11-mCherry, Cmp7-AID and OsTIR1$_{F74A}$ were treated for 1 h with DMSO or 5-adamantyl-IAA (5IAA) followed by EMM5S media with or without 2.5% 1,6-HD for 45 to 90 min—treatments indicated by pluses—before imaging. Post-imaging, cells were categorized by cell cycle stage and analyzed. At the top of each panel are representative images of an ROI that encompasses a nucleus with MGM4, Cut11-mCherry and merged images arranged vertically. Scale bar, 1 µm. At bottom, histograms of N/C ratios of MGM4 fluorescence of individual cells in untreated (gray), 5IAA (yellow), 2.5% 1,6-HD (teal), and both 5IAA and 2.5% 1,6-HD (orange). Percent of values above 0.75 bin (dotted gray line) for each reporter indicated. Size between bins, 0.05. Quantification was performed for three biological replicates N = 955, with at least 197 cells/condition, and at least 50 cells/biological replicate.

H: DMSO or 5IAA-treated cells (MKSP3699) at indicated cell cycle stages expressing MGM4, Cut11-mCherry, Cmp7-AID and OsTIR1$_{F74A}$ were subjected to timelapse imaging after the addition of 2.5% 1,6 HD delivered by microfluidics. For G_2 and G_1/S cells, time 0 indicates the start of imaging after the delivery of 1,6-HD by microfluidics. For mitotic cells, only cells that went through mitosis after 1,6-HD treatment were considered. Images of representative nuclei at each timepoint are shown arranged vertically with MGM4 (green) at top, Cut11-mCherry (magenta) in middle and merge at bottom. Scale bar, 1 µm. Representative of N=360, 20 cells/replicate/cell cycle phase/treatment.

I: Scatterplot of the percent change of MGM4 N/C ratios of individual cells (MKSP3699, either DMSO or 5IAA-treated) expressing MGM4, Cut11-mCherry, Cmp7-AID and OsTIR1$_{F74A}$ from start to end of timelapse imaging after addition of 2.5% 1-6 HD. Bars and error bars represent mean and standard deviation, respectively. Kruskal-Wallis test performed across all cell cycle phases with Dunn's multiple comparisons for each data set against G_2 for the corresponding treatment (****, $p < 0.0001$; ns, $p \geq 0.05$). N=360, 20 cells/replicate/cell cycle phase/treatment.

treatment led to the equilibration of MGM4 fluorescence across the NE in about 20 minutes in WT G_2 cells (Figures 5B and 5C), indicating disruption of the NPC diffusion barrier. Interestingly, upon 5% 1,6-HD addition MGM4 fluorescence equilibrated approximately twice as fast in mitotic cells (Figures 5B and 5C). This observation hints that either the NPC diffusion barrier is weakened during mitosis or there is an additional proteinaceous NE diffusion barrier required during mitosis that is also sensitive to 5% 1,6-HD.

357 Building on a model where there is a mitotic-specific NE diffusion barrier, we
358 reasoned that such a barrier would be vulnerable to the loss of Cmp7, which leads to a
359 much larger NE hole in anaphase B (Figures 3F and 3I). To test this, we turned to an
360 auxin-induced degron (AID) to quickly deplete an endogenously expressed Cmp7-AID
361 fusion, which allowed us to specifically test the impact of the loss of Cmp7 during mitosis
362 (Kanke et al., 2011; Zhang et al., 2022). Cmp7-AID was efficiently degraded within 15
363 minutes of treatment with 5-adamantyl-IAA (5IAA) (Supplementary Figure S3B).
364 Importantly, depletion of Cmp7-AID recapitulates phenotypes observed in *cmp7Δ* cells,
365 for example abolishing recruitment of Ist1-GFP to the NE (Supplementary Figure S3C).
366 Further, like *cmp7Δ*, there was no discernable change in MGM4 N/C fluorescence ratios
367 in 5IAA-treated Cmp7-AID cells (Figures 5D–5G).
368 We therefore sought to specifically disrupt the putative mitotic diffusion barrier in
369 Cmp7-AID depleted cells with 2.5% 1,6-HD, which is insufficient to disrupt the NPC
370 diffusion barrier even during mitosis (Figures 5B–5D, and 5H). Strikingly, treatment of
371 Cmp7-AID depleted cells with 2.5% 1,6-HD resulted in nuclear entry of MGM4 in 56% of
372 late anaphase B cells and 24% of early G_1/S cells but did not impact MGM4 distribution
373 in G_2 cells (Figures 5D–5G). To confirm that the nuclear entry of MGM4 occurred
374 specifically during mitosis under conditions of Cmp7 depletion, we monitored MGM4
375 localization in Cmp7-AID cells (with or without 5IAA) alongside the temporally controlled
376 delivery of 2.5% 1,6-HD in a microfluidic chamber (Figures 5H and 5I). As shown in Figure
377 5H, only mitotic cells depleted of Cmp7-AID in the presence of 2.5% 1,6-HD allowed entry
378 of MGM4 into the nucleus, which we quantified as the percent change in N/C fluorescence
379 ratios of individual cells from the beginning to the end of the experiment (Figure 5I).
380 Together, these data suggest that Cmp7 contributes to a mitotic diffusion barrier
381 independent of NPCs that is distinct from its role in NE membrane sealing.
382
383 ***CMP7* genetically interacts with genes encoding SPB components**
384 We next sought to identify the protein(s) that help form a diffusion barrier capable
385 of preventing macromolecules from transiting a NE hole as large as ~500 nm. Based on
386 the CLEM data, which showed the SPB and a zone of ribosome exclusion covering even
387 the largest NE holes in *cmp7*Δ cells (Figure 3), SPB components were the most likely

A

Genetic interaction of SPB genes with *CMP7*		
Category of encoded protein	Gene	Growth compared to single allele mutants
Constitutive SPB association	*CUT12*	Synthetic lethal
	ALP4	Synthetic sick
	ALP6	Synthetic sick
	ALP14	Synthetic sick
	CAM1	Synthetic sick
	CDC11	Synthetic sick
	GTB1	Synthetic sick
	MZT1	Synthetic sick
	PCP1	Synthetic sick
	SAD1	Synthetic sick
	KMS2	None observed
	MTO1	None observed
	MTO2	None observed
	SID4	None observed
Localized to SPB in mitosis	*BRR6*	Synthetic sick
	CUT11	Synthetic sick
	PLO1	Synthetic sick

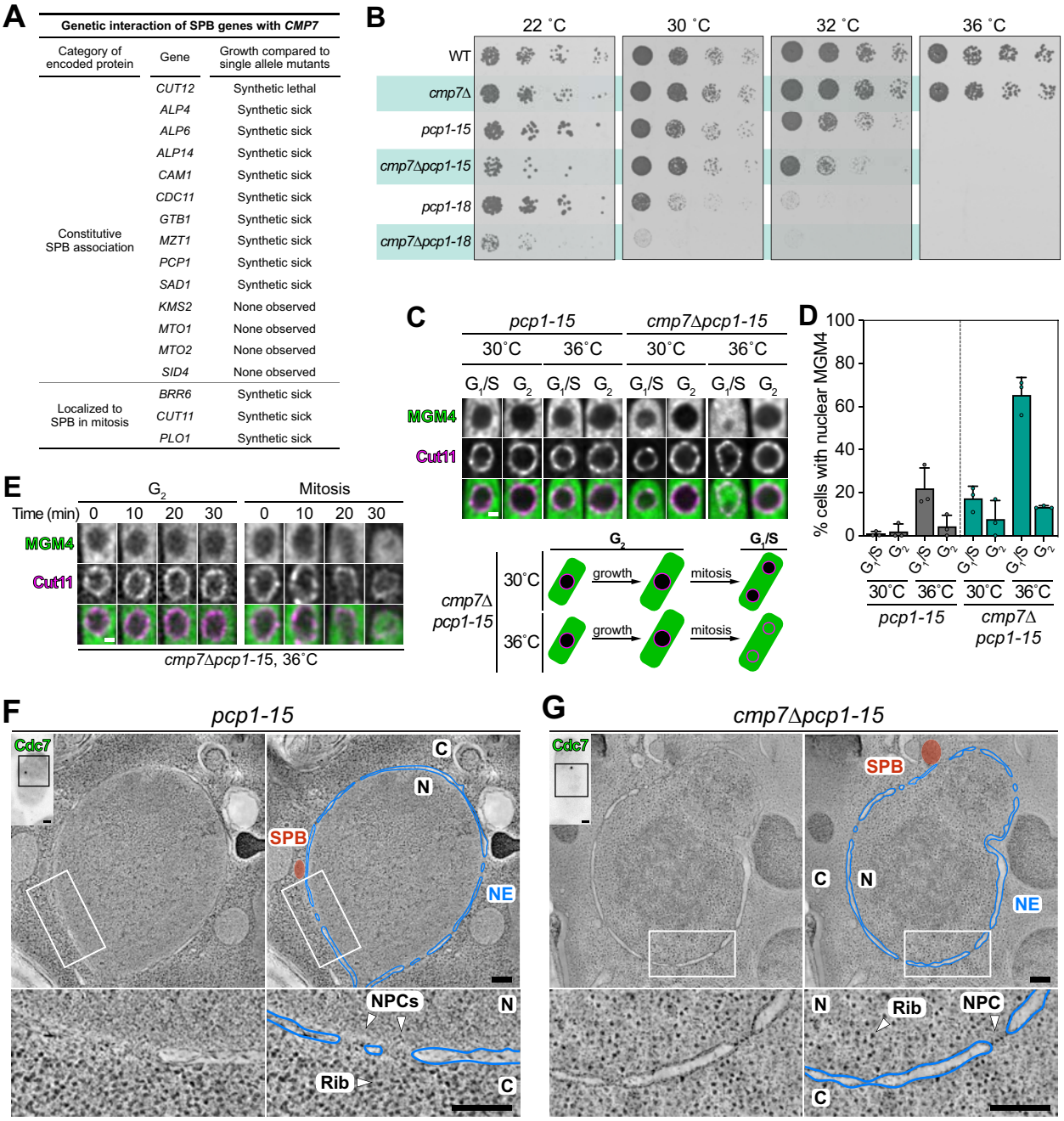

Figure 6. Genes encoding constitutive SPB proteins and mitotically associated SPB proteins genetically interact with *CMP7* and their perturbation leads to loss of nuclear integrity.

Figure legend continued next page.

candidates. We conducted a genetic interaction screen between genes that encode proteins that are either constitutively or transiently (during mitosis) associated with the SPB and *CMP7* (Jaspersen, 2021; Wälde and King, 2014) (Figure 6A, B and Supplementary Figure S4). Of the 17 genetic backgrounds with perturbations to the SPB, 12 were synthetically sick when combined with the *cmp7Δ* allele and one was

Figure 6. *CMP7* is required for robust fitness and nucleocytoplasmic compartmentalization in the context of perturbed SPB protein function.

A: Summary table of observed synthetic genetic interactions from plate growth assay data shown in Supplementary Figure S4.

B: *CMP7* is required for fitness of strains with *PCP1* mutant alleles. The indicated strains were serially diluted 10-fold and plated on YE5S plates incubated at the indicated temperatures. Plates were imaged after 2 days (30, 32, and 36˚C) or 5 days (22˚C). WT, MKSP399; *cmp7*Δ, MKSP3340; *pcp1-15*, MKSP280; *cmp7*Δ*pcp1-15*, MKSP3420; *pcp1-18*, MKSP281; *cmp7*Δ*pcp1-18*, MKSP3425.

C: Fluorescence micrographs of representative nuclei are shown arranged vertically with MGM4 (green) at top, Cut11-mCherry (magenta) in middle and merge at bottom of either *pcp1-15* (MKSP3812) or *cmp7*Δ*pcp1-15* (MKSP3811) strains. Cells were grown at 30˚C then imaged directly or following 3 h at 36˚C. Scale bar, 1 µm. Cartoon model of loss of nuclear integrity as it occurs mostly in post-mitotic G_1/S *cmp7*Δ*pcp1-15* cells grown at 36˚C for 3 h.

D: Plot of the percentage of *pcp1-15* (gray bars, MKSP3812) or *cmp7*Δ*pcp1-15* (teal bars, MKSP3811) MGM4-expressing cells with N/C fluorescence ratios greater than 0.75 reflecting a loss of nucleocytoplasmic compartmentalization. Points are the mean from each biological replicate, while bars and error bars represent total mean and standard deviation, respectively. Points represent average of at least 30 nuclei/cell cycle phase/strain/replicate, N = 977.

E: Fluorescence micrographs of representative nuclei are shown arranged vertically with MGM4 (green) at top, Cut11-mCherry (magenta) in middle and merge at bottom from individual *cmp7*Δ*pcp1-15* cells (MKSP3811) in G_2 or through a timecourse (in minutes) after a temperature shift from 30˚C to 36˚C. Scale bar, 1 µm.

F, G: Top-left inset, fluorescence micrograph of a thick section of a resin-embedded yeast strain (MKSP4107, F; MKSP4106, G) expressing Cdc7-GFP (green) prepared for CLEM and ET following 3 h of incubation at 36˚C. The black square in the fluorescence micrographs indicates regions where the electron tomogram was collected. Left and right panels are a virtual slice taken from the electron tomogram shown without (left) and with (right) manual annotation of features. White square shows magnified region shown in bottom panels. NE, blue, SPB region, red. White arrowheads, NPC. N, nucleus; C, cytoplasm; Rib, ribosomes. Scale bars: fluorescence micrographs, 1 µm; virtual slices from electron tomogram, 200 nm.

394 synthetically lethal. The remaining four alleles that did not rely on *CMP7* for fitness
395 affected proteins that are peripherally associated with the SPB rather than residing in the
396 core structure. Importantly, we find genetic interactions not just between *CMP7* and genes
397 encoding constitutive SPB proteins, but with genes that encode proteins that transiently
398 associate with the SPB to ensure proper mitotic progression (*BRR6*, *CUT11*, and *PLO1*)
399 (Tamm et al., 2011; Wälde and King, 2014; West *et al.*, 1998). Thus, growth (and in some
400 cases viability) of cells with a compromised SPB is dependent on *CMP7*.
401

402 **Cmp7 cooperates with SPB proteins to maintain a NE diffusion barrier during**
403 **mitosis**

404 We next investigated if the loss of fitness of cells lacking Cmp7 and fully functional
405 SPB proteins could be attributed to a specific disruption of a mitotic NE diffusion barrier.
406 To address this, we analyzed the distribution of MGM4 in several genetic backgrounds in

407 which SPB components were perturbed using both temperature sensitive alleles such as
408 *pcp1-15* (Figure 6C) or rapid depletion (1 h after 5IAA addition) in strains expressing AID-
409 fusions of Pcp1 or Ppc89, another core SPB protein (Supplementary Figure S5). We first
410 tested MGM4 localization in *pcp1-15* and *cmp7Δpcp1-15* cells grown at 30˚C and after
411 incubation for 3 h at 36˚C, the non-permissive temperature for the *pcp1-15* allele (Figure
412 6C). At 30˚C MGM4 was excluded from the nucleus with N/C fluorescence ratios <0.75
413 in most cells (Figures 6C and 6D). While cells harboring the *pcp1-15* allele that likely
414 transited mitosis at 36˚C were slightly more likely than WT cells to display aberrant
415 nuclear MGM4 fluorescence in the subsequent G_1/S (~20% of cells had N/C ratios >0.75),
416 the concomitant absence of Cmp7 led to a far more penetrant phenotype (65% of
417 *cmp7Δpcp1-15* G_1/S cells had N/C ratios >0.75) (Figure 6C and 6D). We confirmed that
418 the MGM4 entered the nucleus specifically during the preceding mitosis by timelapse
419 imaging of *cmp7Δpcp1-15* cells during a temperature shift from 30˚C to 36˚C. Strikingly,
420 91% (N=75) of cells with nuclei that became permeable to the MGM4 reporter during this
421 time course were undergoing mitosis (Figure 6E).

422 The Cmp7-dependent loss of nucleocytoplasmic compartmentalization in *pcp1-15*
423 cells was largely mirrored by the conditional depletion of either Pcp1-AID or Ppc89-AID.
424 In these cases, however, simply appending the AID protein domain to Pcp1 and Ppc89
425 sensitized these strains to loss of Cmp7 and resulted in the nuclear entry of MGM4
426 specifically in *cmp7Δpcp1-AID* and *cmp7Δppc89-AID* G_1/S cells. Critically, we find that
427 depletion of Pcp1-AID and Ppc89-AID manifests in loss of the NE diffusion barrier
428 (Supplementary Figure S5B, S5C, S5E, and S5F) prior to leading to mitotic SPB and/or
429 spindle defects (Supplementary Figure 5G–5H), although phenotypes such as monopolar
430 spindles do eventually arise in the population (Supplementary Figure 5I). This surprising
431 result suggests that the canonical role of these SPB proteins in organizing the mitotic
432 spindle (Flory et al., 2002; Fong et al., 2010; Rosenberg et al., 2006) may be secondary
433 to their role in maintaining a mitotic NE diffusion barrier.

434 Lastly, to provide additional insight into the loss of compartmentalization when we
435 combine perturbations of Cmp7 and Pcp1 we performed CLEM of *cmp7Δpcp1-15* cells
436 following 3 h at the restrictive temperature (36˚C). We observed that in half (N=6) of the
437 *cmp7Δpcp1-15* cells examined, and none of the *pcp1-15* cells (N=6), there was a failure

438 to exclude ribosomes from the nucleoplasm (Figure 6F and 6G, magnified boxes) in the
439 presence of an otherwise intact NE. Thus, in aggregate our data strongly suggest that
440 maintaining robust nucleocytoplasmic compartmentalization during mitosis requires
441 cooperation between Cmp7 and functional SPB proteins. Moreover, these data further
442 demonstrate that NPCs are not the sole proteinaceous diffusion barriers that function at
443 the *S. pombe* NE.
444

445 **DISCUSSION**

446 Here we develop and exploit the fission yeast *S. pombe* as a model of ESCRT function
447 at the NE (Supplementary Figure S6). The data firmly establish that ESCRTs are required
448 to seal the NE hole generated by the extrusion of the SPB. Critically, however, we also
449 propose a new function for ESCRTs prior to sealing in which they act as a molecular
450 grommet that restricts the size of the persistent NE fenestration during anaphase B. This
451 grommet function is needed to support a proteinaceous diffusion barrier that is essential
452 to maintain nucleocytoplasmic compartmentalization. Thus, in addition to extending the
453 functional repertoire of ESCRTs, we also introduce the exciting concept that, beyond the
454 NPC, there are other protein diffusion barriers that restrict the passage of
455 macromolecules across the NE.

456 Using genetic and functional assays we identify core components of the SPB as
457 essential to a diffusion barrier that acts in concert with the ESCRT grommet at the NE in
458 fission yeast mitosis (Figure 6). While such a function has not been described previously,
459 the well-established concept that the nuclear compartment is defined by NPCs requires
460 that the constitutively inserted SPB in budding yeast (Byers and Goetsch, 1975; O'Toole
461 et al., 1999) is also capable of restricting the diffusion of macromolecules. Taken together,
462 we think it likely that core SPB components across divergent yeasts possess a
463 fundamental physiochemical property that allows them to constitute a diffusion barrier,
464 which intuitively had to evolve coincident with the adoption of closed mitosis.

465 Our data thus highlight a broader theme, together with published work, in which
466 ESCRTs and proteinaceous diffusion barriers act in concert to protect the integrity of the
467 nuclear compartment. A clear corollary, for example, is how the NPC diffusion barrier
468 installed during NPC biogenesis is supported by the ESCRT pathway in the event that
469 NPC biogenesis fails (Thaller *et al.*, 2019; Thaller *et al.*, 2021; Webster *et al.*, 2014;
470 Webster *et al.*, 2016). Another example might include the rapid recruitment of barrier to
471 autointegration factor (BAF) to exposed chromatin at induced NE ruptures (Halfmann *et*
472 *al.*, 2019). As BAF forms a cross-linked mesh network that can restrict the passage of
473 macromolecules 500 kDa/49 nm in size (Samwer et al., 2017), it is possible BAF together
474 with other factors (including lamin C (Kono et al., 2022)), might plug NE holes quickly
475 before the membranes themselves are later sealed through a mechanism involving LEM

476 protein(s) and ESCRTs. A similar function could be served by galectin, which appears
477 capable of forming biomolecular condensates (Chiu et al., 2020) and recruiting ESCRT-
478 III (Jia et al., 2020) to prevent leakage of lysosomal hydrolases during ESCRT-mediated
479 repair of lysosome membranes (Radulovic et al., 2018; Skowyra et al., 2018).
480 Exactly what physiochemical mechanism(s) underlie the ability of the SPB to form
481 a diffusion barrier remains unclear. One attractive mechanism to form this barrier would
482 be through a biomolecular condensation similar to the canonical diffusion barriers acting
483 at the NE, i.e. the FG-nucleoporins residing in the central channel of NPCs (Celetti et al.,
484 2020; Frey et al., 2006; Petri et al., 2012). Indeed, like NPCs (Ribbeck and Görlich, 2002;
485 Riquelme Barrientos *et al.*, 2023; Shulga and Goldfarb, 2003) and many other liquid or
486 hydrogel-like biomolecular condensates (Kroschwald et al., 2017), we find that the
487 diffusion barrier that supports the maintenance of nuclear compartmentalization in late
488 mitosis is sensitive to relatively low concentrations of 1,6-HD (Figure 5). Further, as this
489 diffusion barrier must be able to form over NE holes that span from tens to hundreds of
490 nanometers in diameter (Figure 3), it must possess a plasticity that could be consistent
491 with an unstructured biomolecular condensate. A key candidate that might contribute to
492 such a function may be Pcp1, as its human ortholog, pericentrin, can undergo
493 biomolecular condensation as a component of the pericentriolar material surrounding
494 centrosomes (Feng et al., 2017; Jiang et al., 2021; Woodruff et al., 2017; Zwicker et al.,
495 2014). We note, however, that we previously demonstrated that Pcp1 molecules
496 incorporated into the SPB behave essentially as a solid material, undergoing little to no
497 turnover with the soluble Pcp1 pool (Wälde and King, 2014). Thus, we cannot rule out
498 that the diffusion barrier identified here could also be created through a more structured,
499 mesh-like mechanism, similar to what has been proposed for BAF (Samwer *et al.*, 2017).
500 Future work will be needed to explore the physiochemical properties of this barrier more
501 fully and exactly how various proteins, such as those identified here, contribute.
502 That the diffusion barrier we identify is sensitive to ESCRT perturbation is
503 presumably because larger holes put greater reliance on this proteinaceous plug. Building
504 on this, we propose that ESCRTs act as a molecular grommet that restricts the size of
505 the NE hole during anaphase B to a scale that can be effectively supported by the
506 diffusion barrier. Superficially, this grommet model has similarities to the “O-ring seal”

507 model that has been suggested to reside at sites of reforming NE surrounding
508 kinetochore-attached microtubules in mammalian cells (von Appen *et al.*, 2020). The
509 concept of an O-ring is primarily based on the formation of a ring-shaped CHMP7-LEM2
510 co-polymer that is observed surrounding microtubules *in vitro* (von Appen *et al.*, 2020)—
511 the structure formed *in vivo* remains unknown. However, our quantitative analysis reveals
512 that only ~16 molecules of Cmp7 reside at the NE hole in anaphase B (Table 1 and
513 Supplementary Figure S2), far less than would be necessary to line the 50–150 nm NE
514 hole (corresponding to the widths measured when Cmp7 is recruited to the SPB extrusion
515 site; Figure 3) if it forms a co-polymer analogous to that suggested for the mammalian
516 CHMP7-LEM2 (von Appen *et al.*, 2020). We suggest that the grommet model outlined
517 here is distinct, favoring instead the possibility that Cmp7 (the sequence of which contains
518 elements of both ESCRT-II and ESCRT-III family members) is a seed filament for the
519 assembly of additional downstream ESCRTs, akin to models that suggest a sequential
520 assembly order of ESCRT-IIIs at endosomes (Babst et al., 2002; Henne et al., 2012;
521 Pfitzner et al., 2020; Saksena et al., 2009; Teis et al., 2008) as well as other contexts that
522 begin with ESCRT-I and ESCRT-II proteins (Vietri *et al.*, 2020). Such a model predicts
523 that Cmp7 is required for all ESCRT recruitment to the NE, which is indeed the case
524 (Figure 2). As CHMP7 is also required for ESCRT subunit recruitment to the NE in
525 mammalian cells at mitotic exit (Gu *et al.*, 2017; Olmos *et al.*, 2016), we suggest that the
526 fundamentals of ESCRT recruitment and function in *S. pombe* and mammalian cells are
527 highly similar. Subtleties between the two models will need to be revealed in future studies
528 that examine the copy number of ESCRTs at well-defined NE holes in mammalian cells
529 in the manner that we have performed here.

530 Although the observed copy number of Cmp7 molecules indicates that they may
531 not be able to independently line a 50–150 nm NE hole, they may nonetheless be
532 constituents of a more complex polymer that includes the Wave 2 ESCRTs, Vps32 and
533 Ist1, which are found at much higher copy numbers than Cmp7 (Table 1 and
534 Supplementary Figure S2). Indeed, based on the recruitment timing (Figure 1) and its
535 relationship to the normal constriction of the NE hole (Figure 3), we infer that a polymer(s)
536 consisting of Wave 1 and 2 ESCRTs comprises the grommet. This grommet appears to
537 restrict the NE hole diameter to support the SPB protein-dependent diffusion barrier

538 (Figure 6). However, as we observe that the NE hole shrinks from 150 nm to 50 nm during
539 the Wave 1 and 2 recruitment period, it is also possible that the grommet is responsible
540 for physically driving its constriction. We speculate that this function could be attributed
541 to Ist1, which is thought to contribute to ILV neck constriction prior to membrane scission
542 during ILV formation (McCullough et al., 2015; Nguyen et al., 2020; Pfitzner *et al.*, 2020),
543 with the caveat that the dimensions of a constricting ILV is an order of magnitude smaller
544 than the NE hole. This comparison further highlights a key difference between the order
545 of assembly/composition of ESCRTs at the NE compared to at endosomes, where Ist1 is
546 instead recruited much later than Vps32 (Pfitzner *et al.*, 2020). Ultimately, a model of
547 membrane fission at the NE must incorporate this difference, as well as the apparent
548 absence of the ESCRT-III Did2; we note, however, that the mammalian Did2 ortholog,
549 CHMP2A, was reported to localize to the reforming NE at mitotic exit (Vietri *et al.*, 2015),
550 opening up the alternative possibility that the levels of Did2-GFP present are below our
551 threshold of detection (Supplementary Figures S1A and S1B).

552 Our data clearly underscore that ESCRTs are required for the penultimate step of
553 NE sealing, likely through a membrane fission mechanism (Figure 3). However, our
554 observation of NE holes as small as 20 nm in the absence of Cmp7 suggests ESCRT-
555 independent mechanisms capable of minimizing the persistent NE hole in G_2, possibly
556 involving local lipid synthesis or flow of membrane from the ER (Kinugasa et al., 2019;
557 Kume et al., 2019; Penfield *et al.*, 2020); normal nucleocytoplasmic compartmentalization
558 in this context further suggests the presence of a functional barrier to diffusion residing in
559 the persistent NE hole. Interestingly, our data also support that the NE sealing mechanism
560 requires maturation of the ESCRT filament including a wholesale replacement from a
561 Cmp7-Vps32-Ist1 grommet in late anaphase B to a NE sealing modality consisting of
562 Vps24 and Did4 in the subsequent G_1/S (Figures 2 and 4). Indeed, temporally, the release
563 of Cmp7 occurs in concert with recruitment of the Wave 3 ESCRTs (Figure 1). We
564 postulate that Cmp7 acts as a seed that initiates a sequence of ESCRT recruitment
565 events, ultimately leading to a mature state of a Wave 3 ESCRT filament that drives NE
566 sealing. Disrupting Wave 3 ESCRTs (Vps24 or Did4) drives the persistence of a Wave 1
567 state in which Cmp7 is found at an abnormally high copy number, apparently stuck in the
568 NE hole that fails to seal (Figures 2 and 4).

569 The observations that both disrupting ESCRT recruitment (*cmp7*Δ cells, Figure 3)
570 or accumulating a stalled ESCRT assembly (*did4*Δ cells, Figure 4) compromise NE
571 sealing has several implications for interpreting how loss of function of ESCRTs manifest
572 more generally. As nucleocytoplasmic compartmentalization can appear grossly normal
573 despite the persistence of these small NE holes, their presence may be undetected by
574 monitoring reporter proteins (Figure 5A). Thus, these observations highlight that it will be
575 important to revisit data suggesting ESCRT-independent NE sealing mechanisms that
576 did not include ultrastructural analysis. Perhaps most importantly, we think it likely that
577 persistent NE holes could lead to an unstable NE barrier that is more susceptible to further
578 perturbation. As loss of Cmp7 and persistent Cmp7 converge in precipitating a failure of
579 NE sealing, this work provides a useful framework to interpret the consequences of
580 ESCRT loss or gain of function in the context of disease. For example, variants in the
581 CHMP2B gene (ortholog of Did4) cause frontotemporal dementia (Skibinski et al., 2005)
582 and the aberrant nuclear entry of CHMP7 is upstream of a pathological cascade that could
583 contribute to both sporadic and familial forms of amyotrophic lateral sclerosis (Coyne et
584 al., 2021). In both scenarios, it is possible that improper clearance of CHMP7 could
585 compromise the integrity of the NE over timescales beyond that easily monitored in cell
586 culture. Further, it will be interesting to examine if some cancer cells are prone to repeated
587 nuclear ruptures due to NE nanoholes arising from inefficient ESCRT-mediated repair,
588 rendering them more fragile.
589

590 **ACKNOWLEDGEMENTS**

591 We thank the Center for Cellular and Molecular Imaging, Electron Microscopy Facility at
592 Yale School of Medicine for assistance with EM, particularly Morven Graham and Xinran
593 Liu. Additionally, we thank Li-Lin Du, Adam Frost, Iain Hagan, Tom Pollard, and NBRP
594 (YGRC), Japan for yeast strains. This work was supported by the National Institutes of
595 Health (R01 GM105672 to C.P. Lusk; F32 GM139285 to N.R. Ader) and an Allen
596 Distinguished Investigator Award, a Paul G. Allen Frontiers Group advised grant of the
597 Paul G. Allen Family Foundation (M.C. King).

598

599 **METHODS**

600 ***S. pombe* culture and strain generation.** Strains used in this study are listed in
601 Supplemental Table S2. Strains were cultured and mated using standard procedures and
602 media (Moreno et al., 1991). In brief, *S. pombe* were cultured on yeast extract
603 supplemented with 250 mg/liter adenine, histidine, leucine, uracil, and lysine
604 hydrochloride (YE5S) agar plates and liquid cultures. For experiments with MGM4, cells
605 were grown in Edinburgh minimal medium supplemented with 250 mg/liter adenine,
606 histidine, leucine, uracil, and lysine hydrochloride (EMM5S) overnight prior to imaging. C-
607 terminal tagging and gene replacement (knockout) were performed using the pFA6a,
608 MX6-based drug resistance cassettes (Bahler et al., 1998; Hentges et al., 2005) using *S.*
609 *pombe* genome information available through PomBase (Harris et al., 2022; Wood et al.,
610 2002). Visualization and virtual manipulation of DNA sequences was facilitated by using
611 ApE 2.0.61 (Davis and Jorgensen, 2022). For all GFP fusions, mEGFP was used. For C-
612 terminal tagging of Cmp7 for AID depletion we used pNA55 (pDB4581), a gift from Li-Lin
613 Du (Addgene plasmid # 171124) (Zhang *et al.*, 2022). All genomic integrations were
614 confirmed by screening of individual clones by PCR of whole yeast (colony PCR) (Huxley
615 et al., 1990) with primers designed to amplify only a genomic insertion at the targeted
616 locus following a standard lithium acetate transformation procedure (Murray et al., 2016).

617 As has been previously shown, dysfunctional tagged ESCRT proteins display a
618 loss of dynamic remodeling and aberrantly accumulate in class E endosomes (Teis *et al.*,
619 2008). Thus, to generate functional GFP-ESCRTs, we first attempted C-terminal tagging
620 using a 3×HA linker. For Cmp7-3×HA-GFP, Ist1-3×HA-GFP, and Did2-3×HA-GFP this
621 strategy yielded GFP-ESCRTs which were dynamic by live-cell imaging (Figure 1) and
622 capable of generating progeny when mated. As we noted that expression of Vps32-3×HA-
623 GFP and Did4-3×HA-GFP appeared to drive a dominant negative phenotype that
624 inhibited tetrad formation, we used an N-terminal tagging strategy for tagging of Vps32,
625 Did4, and Vps24. N-terminal GFP-tagging of Vps32, Vps24, and Did4 was performed by
626 inserting a pJK148 plasmid cut with NruI at the *leu1-32* locus in a strain with the
627 endogenous gene knocked out (pNA32 for GFP-3×HA-Vsp32, pNA23 for GFP-3×HA-
628 Vps32, and pNA45 for GFP-3×HA-Did4; see Supplementary Table S2 for full plasmid list)
629 (Keeney and Boeke, 1994). To generate pNA22, pNA23, and pNA45 plasmids, we

630 performed Gibson Assembly of the following sequences: (1) promoter (500 bp upstream
631 of start 5' UTR) + 5'UTR, (2) GFP-3×HA, (3) open reading frame + 3'UTR + terminator
632 (500 bp downstream of stop codon) (Gibson et al., 2009). Strains with GFP-3×HA -Vps32,
633 GFP-3×HA -Vps24, and GFP-3×HA -Did4 had dynamic GFP-ESCRT foci (Figure 1) and
634 had no apparent defect in mating, producing viable tetrads.
635
636 **Live-cell fluorescence microscopy.** Cells expressing fluorescent protein fusions were
637 grown to log phase (OD_{600} 0.4–0.8) in YE5S supplemented with an additional 250 mg/L
638 adenine (to ensure low autofluorescence) and 0.1 mM *n*-propyl gallate (NPG) (an oxygen
639 scavenger to reduce photobleaching and mitochondrial autofluorescence), concentrated
640 by 20 s centrifugation at 2000× *g*, sandwiched between a #1.5 glass coverslip (VWR
641 48393) and a glass slide (Thermo Fischer Scientific 420), and sealed with VALAP (1:1:1,
642 vaseline:lanonin:paraffin). Image acquisition was performed on a DeltaVision microscope
643 (Applied Precision; GE Healthcare) using Resolve3D in SoftWoRx using the Insight SSI
644 4-color Live Cell filter set (ex425–495/em500–550 nm for GFP, ex555–590/em600–675
645 nm for mCherry) on a CoolSNAP HQ^2 CCD (Photometrics) or Evolve-512 EMMCD
646 (Photometrics) with either an UPlanSapo 100× 1.4 NA oil immersion objective (Olympus)
647 or a PlanApo 63× 1.42 NA oil immersion objective (Olympus) and an AURA light engine
648 (Lumencor) at 32% transmission or 100% transmission for up to 1 s. Cells were imaged
649 over 4.8–5 µm in the z-plane at 0.2 intervals for counting, 0.5 µm for compartmentalization
650 (MGM4 and MGM2), and 0.2–0.4 µm for all other experiments. Deconvolution was
651 performed using SoftWoRx; deconvolved images were used only for display, not intensity
652 based analysis. For timelapse experiments with drug delivery, cells were first loaded into
653 a CellASIC ONIX microfluidic plate (Millipore Y04C) before imaging. Microfluidics were
654 controlled by the CellASIC ONIX microfluidic platform (Millipore EV262, MIC230, GM230).
655 For Cmp7-AID depletion, 5IAA (TCI Chemicals, A3390) was dissolved in DMSO to make
656 a 1 mM stock solution and used at a final concentration of 100 nM in culture. For treatment
657 with 1,6-HD, 1,6-hexanediol (Alfa Aesar, A12439) was dissolved in YE5S plus 250 mg/L
658 adenine to make a 25% stock solution, which was diluted to either 2.5% or 5% as needed.
659 Fluorescence micrographs were viewed and analyzed using Fiji 2.3.0/1.53q unless
660 otherwise noted (Schindelin et al., 2012).

661

662 **Image Display**. All representative micrographs have been deconvolved as described
663 above and are displayed to maximize the displayed dynamic range without pixel
664 saturation in the linear range. When mCherry-Atb2 and Pcp1-mCherry or mCherry-Atb2
665 and Sad1-mCherry are displayed together, the gamma has been adjusted to 0.05 to allow
666 both fluorophores to be displayed without pixel saturation. All magnified ROIs of
667 fluorescence micrographs were independently adjusted.

668

669 **Cell cycle classification for GFP-ESCRT localization to SPB extrusion site.** To
670 classify cells into phases of the cell cycle from still images, we used the following criteria:
671 Cells with mitotic spindles longer than 3 µm were considered to be in anaphase B and
672 were converted to time in anaphase B using the following formula:

673 $$\text{Time in anaphase B} = \frac{\text{spindle length (µm)}}{0.70\ \text{µm min}^{-1}} - 4.29\ \text{min}$$

674 We used the rate of spindle elongation of 0.7 µm/min in anaphase B as determined in
675 (Krüger *et al.*, 2019) and the correction factor of 4.29 min represents a spindle length of
676 3 µm at the anaphase A/B transition. Cells with mitotic spindles longer than 3 µm, but
677 smaller than 6.35 µm were classified as early anaphase B (approximately 0–5 min into
678 anaphase B). Cells with spindles between 6.35 µm and 8.39 µm were classified as mid
679 anaphase B (approximately 5–7.5 min into anaphase B) and any cell with a spindle longer
680 than 8.39 µm was classified as late anaphase B (>7.5 min into anaphase B). Late G_1/S
681 cells were distinguished from early G_1/S cells by the lack of microtubules spanning the
682 septum region. For each phase of the cell cycle the percentage of SPB foci (Sad1-
683 mCherry or Pcp1-mCherry) that colocalized with the GFP-ESCRT was quantified for still
684 images as shown in Figures 1C, 2C–E, 2G, and 2I as well as Supplementary Figures S1B
685 and S3C. Quantification was performed across three biological replicates with at least 50
686 nuclei per replicate.

687

688 **Assessing the timing of GFP-ESCRT at SPB in anaphase B.** Strains expressing a
689 GFP-ESCRT protein, a SPB marker (Sad1-mCherry or Pcp1-mCherry), and mCherry-
690 Atb2 were imaged every 3 min for approximately 20 min. For cells entering anaphase B,

691 we recorded the length of the mitotic spindle in the first frame of the time-series where a
692 focus of the GFP-ESCRT could be discerned. These spindle lengths were converted to
693 time in anaphase B using the above formula (Figure 1D). We also used this method to
694 quantify the timing of SPB extrusion and NE constriction (Figure 1D, vertical gray bars).
695 Quantification was performed across three biological replicates with at least 50 nuclei per
696 replicate.
697
698 **Quantification of average copy number of ESCRT-III subunits.** Cells were prepared
699 for imaging by overnight culture in YE5S plus 250 mg/L adenine + 0.1 mM NPG to log
700 phase. Cells (MKSP3186) expressing Fta3-GFP were mounted on the same pad as a
701 GFP-ESCRT-expressing strain of interest. Cells were imaged as above. Raw images
702 were then analyzed using a custom MATLAB script, 'Find_n_Fit_Spots'
703 (https://github.com/LusKingLab/Find_n_Fit_Spots_3D). First, spots were detected using
704 'findIrregularSpots3', a custom-written MATLAB code that finds fluorescent objects
705 regardless of their shape. Briefly, the code identifies all the brightest pixels within sub-
706 volumes of a given size. Then, it calculates the ratio of the mean intensities of "central"
707 pixels over "edge" pixels. If the ratio is above a given threshold, the code keeps the
708 identified spot and calculates its 3D coordinates as an intensity-weighted centroid of
709 pixels. Second, for each "good" spot, x-y-coordinates were used to crop a circular image
710 with R = 7 pixels around the spot from the best 2D image (determined by z-coordinate)
711 which was fitted by the linear combination of a 2D Gaussian and error function, *erf*, to
712 account for nuclear edge background signal. The volume of the best Gaussian fit was
713 then used as a spot intensity. Identified spots were then manually curated to classify the
714 spot (Fta3-GFP or GFP-ESCRT) based on secondary fluorescent markers. Position in
715 the cell cycle was determined using brightfield images and, for GFP-ESCRT strains,
716 mCherry-Atb2. For each GFP-ESCRT focus, the copy number was determined by
717 dividing the intensity of the focus by the average intensity of mitotic Fta3-GFP, previously
718 calculated to be approximately 111 molecules (Lawrimore *et al.*, 2011). For the
719 comparison of Fta3-GFP intensities across cell cycles (Supplemental Figures S2E–S2G),
720 the measured intensity is plotted by position in the cell cycle. To allow comparisons across
721 three biological replicates, individual datapoints were normalized to the average value for

722 each cell cycle position within the replicate. Fta3-GFP or GFP-ESCRT foci identified as
723 outliers using ROUT test Q = 1%, 1 iteration were excluded.
724
725 **Quantification of N/C ratio of fluorescent reporters.** To calculate the ratio of MGM4
726 and MGM2 fluorescent reporters in the in nucleoplasm vs. cytoplasm, we measured the
727 mean intensity of regions within the nucleoplasm, cytoplasm (avoiding vacuoles), and
728 outside of the cells (background). The background mean intensity was subtracted from
729 both the nucleoplasm and cytoplasmic mean intensities before calculating the N/C ratio.
730 The individual N/C ratios were then binned with 0.05 bin size using Microsoft Excel. When
731 these data are displayed as a histogram (Figure 5D–G), where the percentage of nuclei
732 in each bin is shown. For visual simplicity, these data are simplified and displayed as only
733 the percent of cells with nuclear MGM4 (nuclei in bins 0.75 and above; Figure 6D and
734 Supplementary Figures S5C and S5F). For percentage change of N/C ratio in time-series
735 imaging (Figure 5I), the N/C ratio of the first frame of the movie was subtracted from the
736 N/C ratio of the last frame and then divided by the N/C ratio of the first frame.
737 Quantification was performed across three biological replicates with at least 50 cells per
738 replicate.
739
740 **Quantification of MGM4 nuclear fluorescence over time**. To analyze the fluorescence
741 intensity of nuclear MGM4 reporter, we first corrected for photobleaching using the
742 "Bleach Correction" function in Fiji with an exponential fit. For each cell, we measured the
743 mean fluorescence intensity of a region within the nucleoplasm for each frame of a time
744 series. To compare cells within and across populations, background subtracted intensity
745 measurements were normalized to the intensity of the nuclear region in the first frame.
746 Quantification was performed across three biological replicates with at least 5 nuclei per
747 replicate.
748
749 **Quantification of Cmp7-GFP fluorescence intensity in *did4*Δ cells**. To compare the
750 intensity of Cmp7-GFP at the SPB site across the cell cycle, we measured the mean
751 intensity the GFP channel in a background-subtracted circular area. Position in the cell
752 cycle was determined by mCherry-Atb2 morphology. To allow comparisons across three

753 biological replicates, individual datapoints were normalized to the average value for
754 mitotic cells with visible Cmp7-GFP foci. At least 30 cells were analyzed in each of three
755 biological replicates.
756
757 **Correlative light and electron microscopy.** CLEM of resin-embedded cells was
758 performed as described by Kukulski et al. (2012). In brief, cells were grown overnight in
759 YE5S plus 250 mg/L adenine to log phase before being concentrated using either
760 filtration, with a 0.45 µm nitrocellulose membrane (Millipore HAWP02500) and a
761 microanalysis filter setup (Millipore XX1012500) (Figure 3), or centrifugation at 2000× *g*
762 for 20 s (Figure 6F, G). Concentrated cells were transferred using either a blunted
763 toothpick or micropipette to the 200-µm recess of an aluminum platelet (Engineering
764 Office M. Wohlwend 241) (McDonald, 1999). Platelets were then frozen using a high-
765 pressure freezer (Leica Microsystems HPM100). Samples were freeze substituted in 0.1–
766 5% uranyl acetate in acetone and embedded in Lowicryl HM20 (Polysciences) with
767 automated temperature control (Leica Microsystems EM-AFS2), manual agitation and
768 solution exchange. Resin-embedded cells were sectioned to a 250 nm nominal thickness
769 using an ultramicrotome (Leica Artos 3D) equipped with a diamond knife (Diatome) before
770 being collected on 200 mesh copper grids with carbon support (Ted Pella 01840).
771 Fluorescence micrographs of grids were acquired using a DeltaVision microscope
772 with the optical configuration as described above for live-cell imaging. For each grid
773 square of interest, 10 z-sections were acquired every 250 nm with 3 s exposure with GFP
774 and mCherry imaging setup at 32% transmission. 15 nm protein A-coated gold beads
775 (Cell Microscopy Core, University Medical Center Utrecht) were adhered to grids prior to
776 EM to aid in tilt-series alignment prior to tomogram reconstruction.
777 Single or dual-axis tilt series were collected on an electron microscope (FEI TF20)
778 operated at 200 kV using a high-tilt tomography holder (Fischione Instruments 2020) from
779 approximately -60 to +60 degrees (one-degree increments) at a binned pixel size of 1.242
780 nm on a 4k × 4k Eagle CCD (FEI) using a 150 µm C2 aperture and a 100 µm objective
781 aperture in an automated fashion using SerialEM (Mastronarde, 2005). Reconstruction
782 and segmentation were performed using IMOD (Kremer et al., 1996), with the former in
783 an automated fashion (Mastronarde and Held, 2017). For better visibility in shown virtual

784 slices, a nonlinear anisotropic diffusion and Gaussian filter were applied in IMOD.
785 Fluorescence micrographs have been rotated to match the orientation of virtual slices and
786 adjusted for contrast individually.
787
788 **Measurement of NE hole width**. To measure the size of the NE hole at the SPB
789 extrusion site, we recorded the maximum 2D distance between the two pore membrane
790 regions of the NE abutting the SPB through the tomogram in IMOD. As some tomograms
791 captured only part of the NE in the visualized slice, some of these values may be
792 underestimates of the actual hole size (Figure 3I, open circles).
793
794 **Preparation of whole cell protein extracts and immunoblotting.** Overnight cultures of
795 yeast were grown in EMM5S to log phase. Cultures were centrifuged at 2000× *g* for 5 min
796 and cell pellets were washed with 1 mM EDTA. Cells were then pelleted and lysed in 2M
797 NaOH incubated for 10 min on ice. An equal volume of 50% trichloroacetic acid (TCA)
798 was mixed in before incubating for 10 min on ice and collecting the protein precipitate by
799 centrifugation. The pellet was then washed with –20˚C acetone and air-dried for 15 min.
800 The pellet was then dissolved in 5% SDS followed by an equal volume of SDS-PAGE
801 sample buffer containing urea (24 mM Tris-Cl pH 6.8, 9 M urea, 1 mM EDTA, 1% SDS,
802 10% glycerol). Samples were either shaken at 37˚C for 15 min (Supplementary Figure
803 S3B) or incubated at 90˚C for 5 min (Supplementary Figures S5A and S5D) before being
804 centrifuged at 14,000× *g* for 15 min. Approximately equal loads of extracted protein was
805 then resolved on tris-glycine 10% SDS-PAGE gels and transferred using wet transfer to
806 0.2 µm nitrocellulose membrane (Bio-Rad 1620112). Transferred proteins were then
807 stained with Ponceau S Solution (Sigma-Aldrich P3504) before being scanned on a
808 flatbed scanner (Epson V800 Photo). Blots were blocked overnight in blocking buffer (5%
809 (w/v) dry milk/TBST) and incubated with primary mouse α-mAID antibody (MBL M214-3)
810 (diluted 1:1000 in blocking buffer). The blots were then incubated for 1 h at room
811 temperature with secondary HRP-conjugated goat anti-mouse antibodies (Invitrogen
812 3430). Antibody-labeled proteins were visualized using SuperSignal West Femto
813 Maximum Sensitivity ECL Substrate (Thermo Fischer Scientific 34094) on a VersaDoc
814 Imaging System (Bio-Rad 4000 MP) with a 1.4 mm aperture and a three-minute exposure

time. Digital images of blots were processed using the “Despeckle” function in Fiji and then adjusted to maximize intensity range without over- or under-saturation.

Plate-based growth assays. To evaluate relative colony growth rates, cells were grown overnight in YE5S media. Cells were then diluted to 1 OD_{600} equivalent in YE5S before sequentially plating 5 serial 1:10 dilutions on YE5S plates. The plates were incubated at the indicated temperatures in figures/figure legends and scanned daily on a flatbed scanner (Epson V800 Photo).

Statistical methods. All graphs were generated and analyzed for statistical significance using Prism 9 (GraphPad). Tests used for each figure panel are denoted in figure legends.

Data Availability. The datasets generated during and/or analyzed during the current study are available from the corresponding authors on reasonable request.

Code Availability. MATLAB script for quantification of ESCRT subunits is available here with no access restrictions: https://github.com/LusKingLab/Find_n_Fit_Spots_3D

835 **SUPPLEMENTARY FIGURES**

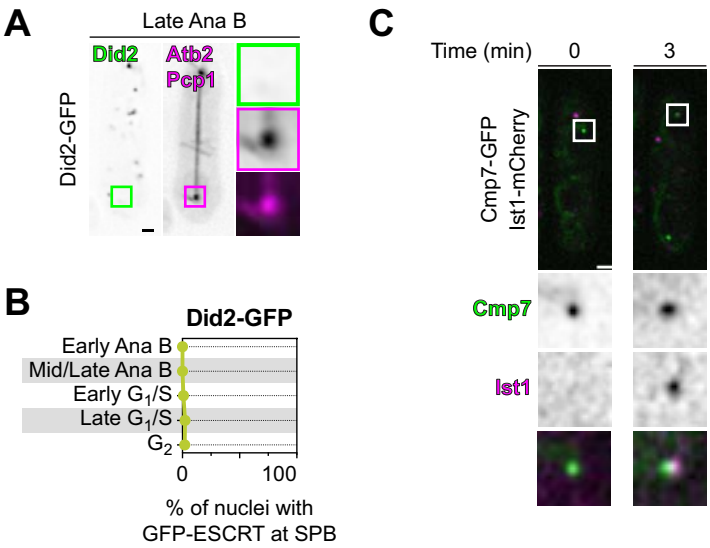

836

Supplementary Figure S1. Did2 is not detected at the SPB extrusion site, while Ist1 is recruited after Cmp7

A: Fluorescence micrographs of Did2-GFP, mCherry-Atb2, and Pcp1-mCherry in a representative cell in anaphase B. Image of the Cmp7-GFP is on left, sum projection (over 4.8 µm) of mCherry-Atb2 in middle and magnifications of square ROI shown vertically arranged at right with (top to bottom) green, magenta and merged channels. Fluorescence intensity of magnified ROIs were independently adjusted in linear range. Scale bar, 1 µm. Magnified ROIs, 1.6 µm wide. To maximize image clarity, fluorescence intensity of magnified ROIs were independently adjusted in the linear range with the exception of the magenta channel where the gamma was adjusted to 0.05 to allow visualization of mCherry-Atb2 and Pcp1-mCherry without saturation.

B: Plot of the percentage of nuclei with Did2-GFP (MKSP3342) colocalized with SPB marker at indicated phases of the cell cycle. Points and error bars represent mean and range, respectively, across at least three biological replicates with at least 50 nuclei/GFP-ESCRT/replicate, N = 372 nuclei.

C: Time-lapse fluorescence microscopy of Cmp7-GFP (green) and Ist1-mCherry (magenta) in a late anaphase B cell (MKSP3521). Cell representative of population from two biological replicates. White boxes in overview micrographs indicate ROI magnified below images as single channel and composite images.

837

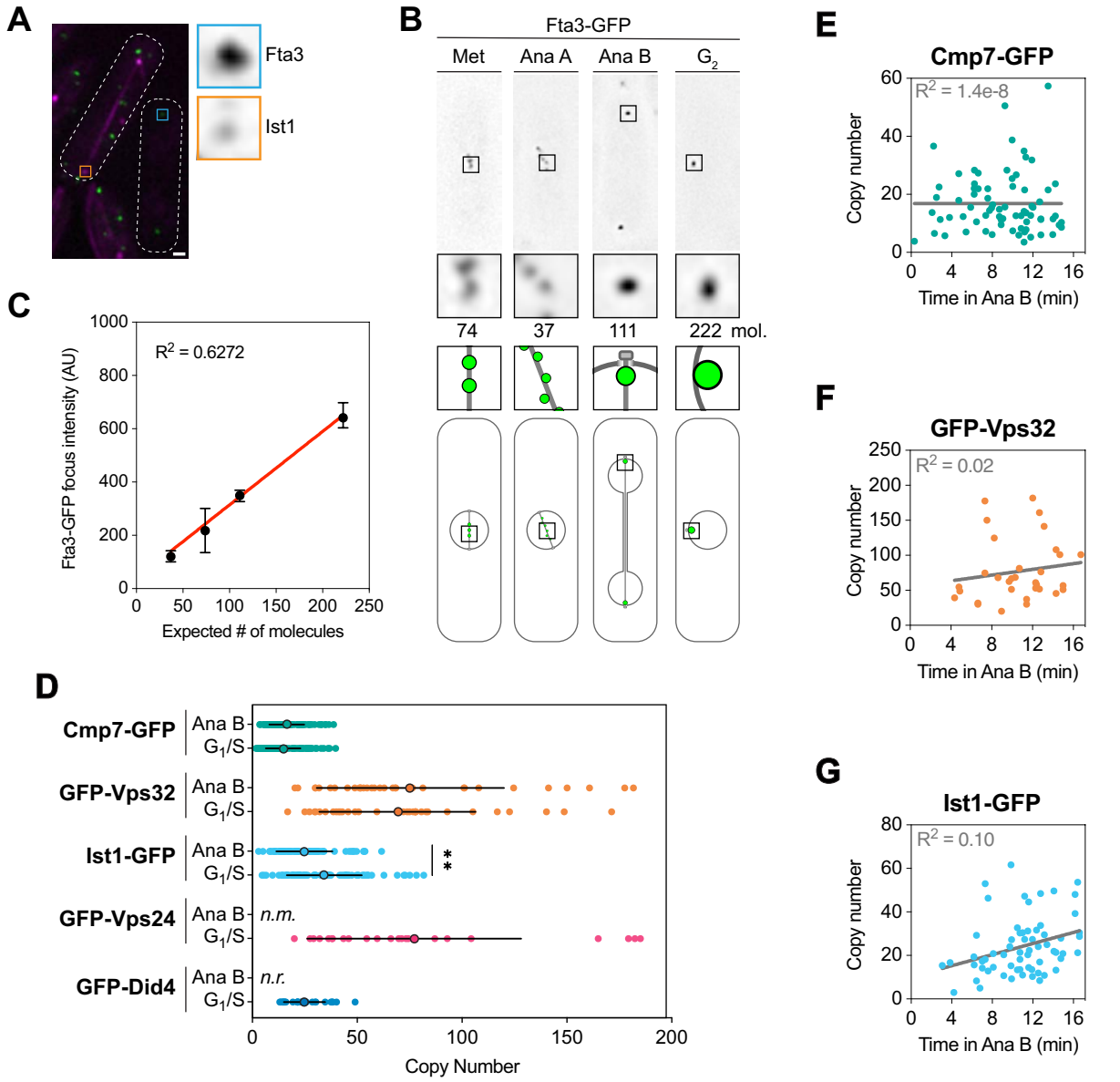

838

Supplementary Figure S2. Average copy number of ESCRTs at the SPB extrusion site determined by ratiometric quantification.

Figure legend continued next page.

839

Supplementary Figure S2. Average copy number of ESCRTs at the SPB extrusion site determined by ratiometric quantification.

A: Fluorescence micrographs of representative mixture of a GFP-ESCRT strain (Ist1-GFP, MKSP3365) and one expressing Fta3-GFP (MKSP3186). In top left, strain expressing Ist1-GFP (green), mCherry-Atb2 (magenta), and Sad1-mCherry (magenta). In bottom right, Fta3-GFP strain (green). Scale bar, 1 µm. Blue and orange boxes in overview micrographs indicate ROI magnified to the right of image as single channel images for Fta3-GFP and Ist1-GFP, respectively.

B: Fluorescence micrographs of representative Fta3-GFP expressing cells (MKSP3186) at indicated cell cycle stage (top). Black boxes in overview micrographs indicate ROI magnified below images (middle). Schematic representation of Fta3-GFP appearance by cell cycle show (bottom). Number of molecules based on Lawrimore et al. (2011).

C: XY plot of Fta3-GFP focus fluorescence intensity against expected number of molecules per focus in MKSP3186 based on Lawrimore et al. (2011). Points represent median of all values collected for that stage of the cell cycle (B); error bars represent 95% confidence interval. Red line represents a simple linear regression with the R^2 shown. N = 366 foci across three biological replicates with at least 50 foci/replicate.

D: Number of molecules of indicated GFP-ESCRT at the SPB extrusion site during all phases of the cell cycle. Outlined point and black lines represent mean and standard deviation, respectively. *n.r.*, not recruited. *n.m.*, not measured. Data was collected over at least three biological replicates. Kruskal-Wallis test performed across all cell cycle phases for each ESCRT individually with Dunn's multiple comparisons across all other cell cycle phases (*, $p < 0.05$; **, $p<0.01$; all others, $p \geq 0.05$). Fta3-GFP (MKSP3186); Cmp7-GFP (MKSP3363), N = 196 foci; GFP-Vps32 (MKSP3353), N = 68 foci; Ist1-GFP (MKSP3365), N = 147 foci; GFP-Vps24 (MKSP3352), N = 24 foci; GFP-Did4 (MKSP3334), N = 26 foci.

E–G: Copy number of indicated GFP-ESCRT shown as a function of time in anaphase B. Gray lines represent a simple linear regression with the R^2 shown in gray. Fta3-GFP (MKSP3186); Cmp7-GFP (MKSP3363), N = 73 foci; GFP-Vps32 (MKSP3353), N = 32 foci; Ist1-GFP (MKSP3365), N = 64 foci.

840

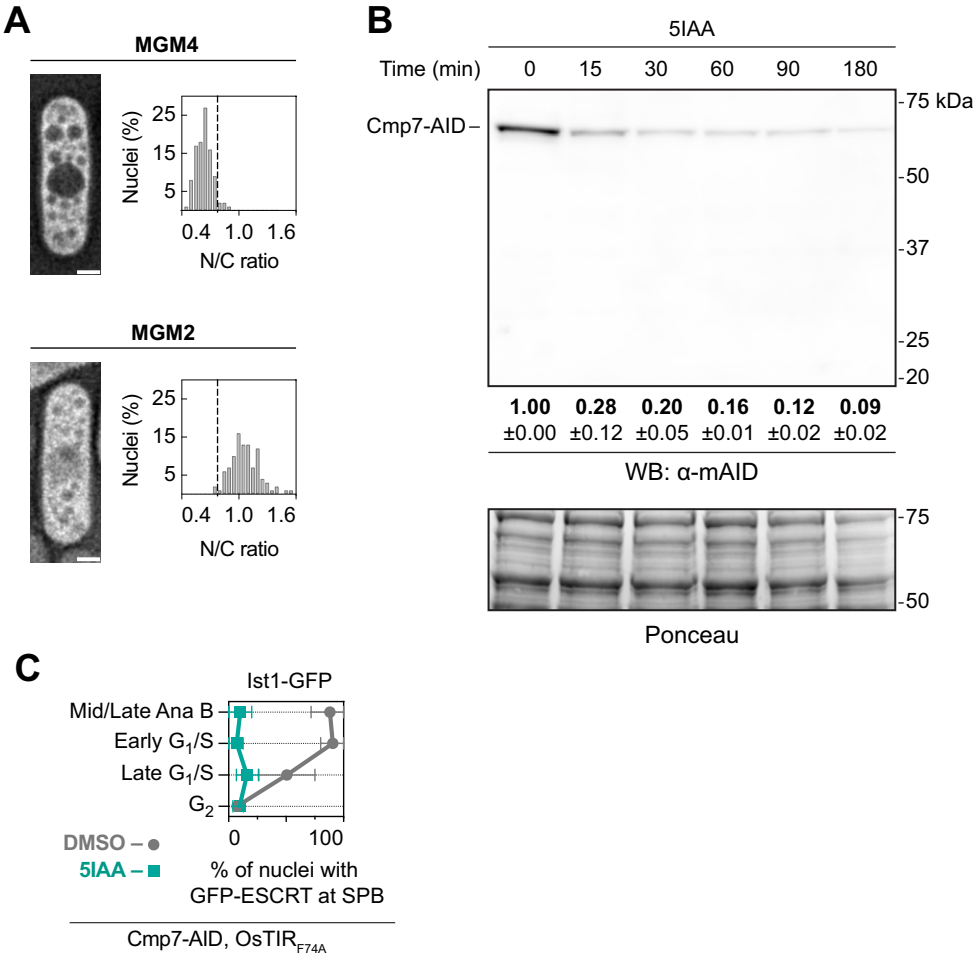

841

Supplementary Figure S3. MGM4 and MGM2 reporters; auxin induced degron (AID) system allows for fast degradation of Cmp7.

A: Deconvolved live-cell fluorescence microscopy of MGM4 (top left, MKSP3345) and MGM2 (bottom left, MKSP3960). Histogram of nucleoplasmic to cytoplasmic GFP fluorescence (N/C ratio) for individual cells shown to the right of each reporter. MGM4 data replotted from Figure 5A. Size between bins, 0.05. Dotted line at 0.75 bin. Quantification was performed for three biological replicates. MGM2, N = 178 nuclei, with at least 58 nuclei/biological replicate.

B: Representative western blot (WB) of Cmp7-AID levels (detected with an α-AID antibody) in total protein extracts from cells (MKSP3517) grown in the presence of 5IAA for the indicated times. Ponceau stain is shown at bottom to assess relative total protein loads. Relative amount of Cmp7-AID protein, normalized to T_0, is shown below WB as mean and standard deviation for three biological replicates.

C: Plots of the percentage of nuclei with Ist1-GFP colocalized with SPB marker at indicated phases of the cell cycle in cells (MKSP3625) expressing Cmp7-AID and $OsTIR1_{F74A}$. Cells were treated with DMSO (gray) or 5IAA (green) for 1 h. Points and error bars represent mean and range, respectively, across at least three biological replicates with at least 50 nuclei/GFP-ESCRT/replicate. DMSO, N = 273 nuclei; 5IAA, N = 296 nuclei.

842

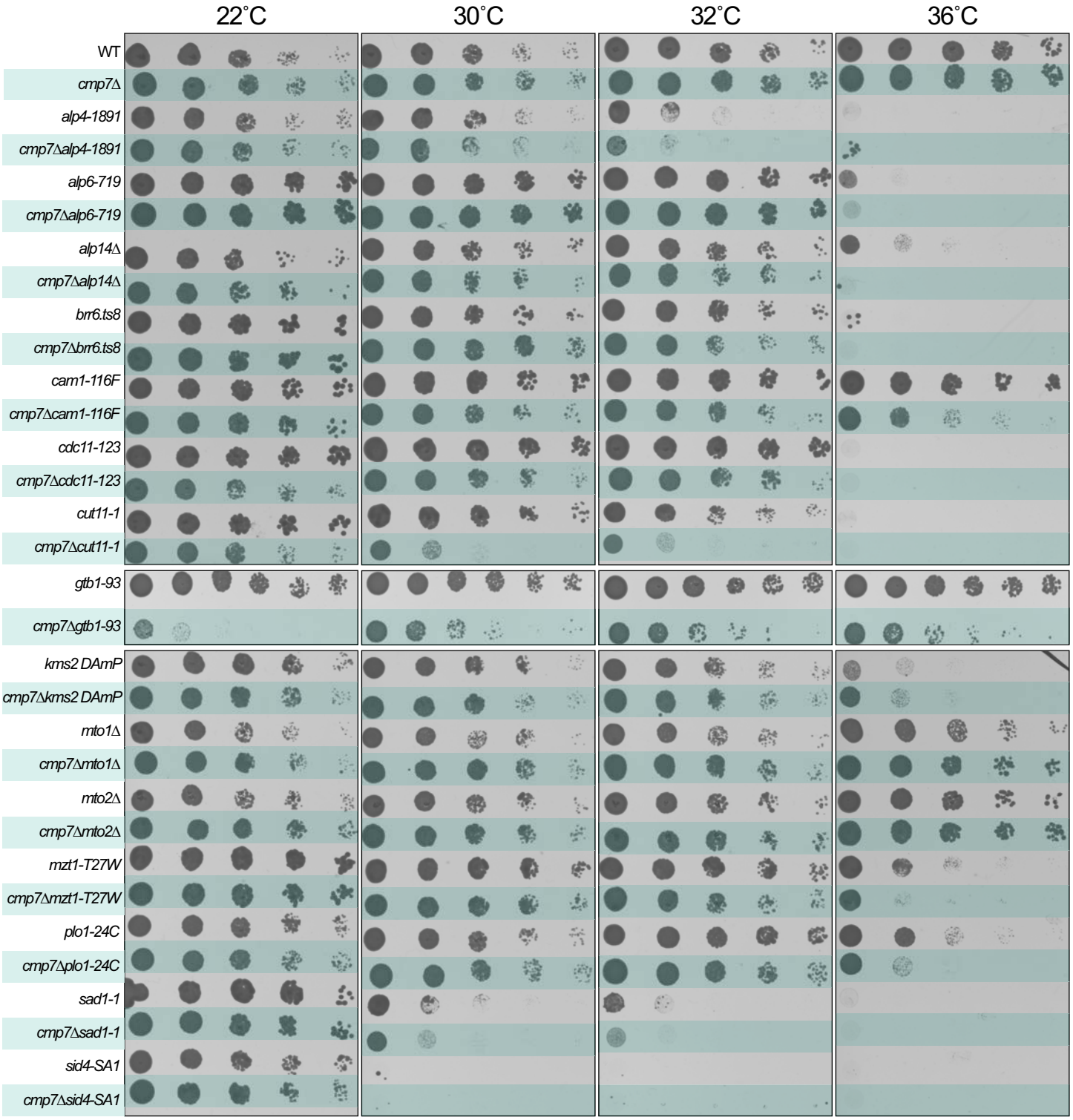

Supplementary Figure S4. Genes encoding constitutive SPB proteins and mitotically associated SPB proteins genetically interact with *CMP7*

The indicated strains were serially diluted 10-fold and plated on YE5S plates incubated at the indicated temperatures. Plates were imaged after 2 days (30, 32, and 36˚C) or 4 days (22˚C). WT, MKSP399; *cmp7*Δ, MKSP3107; *alp4-1891*, MKSP4067; *cmp7*Δ*alp4-1891*, MKSP4163; *alp6-719*, MKSP3475; *cmp7*Δ*alp6-719*, MKSP4031; *alp14*Δ, MKSP4063; *cmp7*Δ*alp14*Δ, MKSP4165; *brr6.ts8*, MKSP3461; *cmp7*Δ*brr6.ts8*, MKSP3528; *cam1-116F*, MKSP4061; *cmp7*Δ*cam1-116F*, MKSP4167; *cdc11-123*, MKSP4060; *cmp7*Δ*cdc11-123*, MKSP4169; *cut11-1*, MKSP3469; *cmp7*Δ*cut11-1*, MKSP4040; *gtb1-93*, MKSP4062; *cmp7*Δ*gtb1-93*, MKSP4174; *kms2 DAmP*, MKSP1474; *cmp7*Δ*kms2 DAmP*, MKSP3683; *mto1*Δ, MKSP1303; *cmp7*Δ*mto1*Δ, MKSP4027; *mto2*Δ, MKSP1305; *cmp7*Δ*mto2*Δ, MKSP4151; *mzt1-T27W*, MKSP3476; *cmp7*Δ*mzt1-T27W*, MKSP4045; *plo1-24C*, MKSP1461; *cmp7*Δ*plo1-24C*, MKSP4048; *sad1-1*, MKSP3468; *cmp7*Δ*sad1-1*, MKSP4033; *sid4-SA1*, MKSP4065; *cmp7*Δ*sid4-SA1*, MKSP4171.

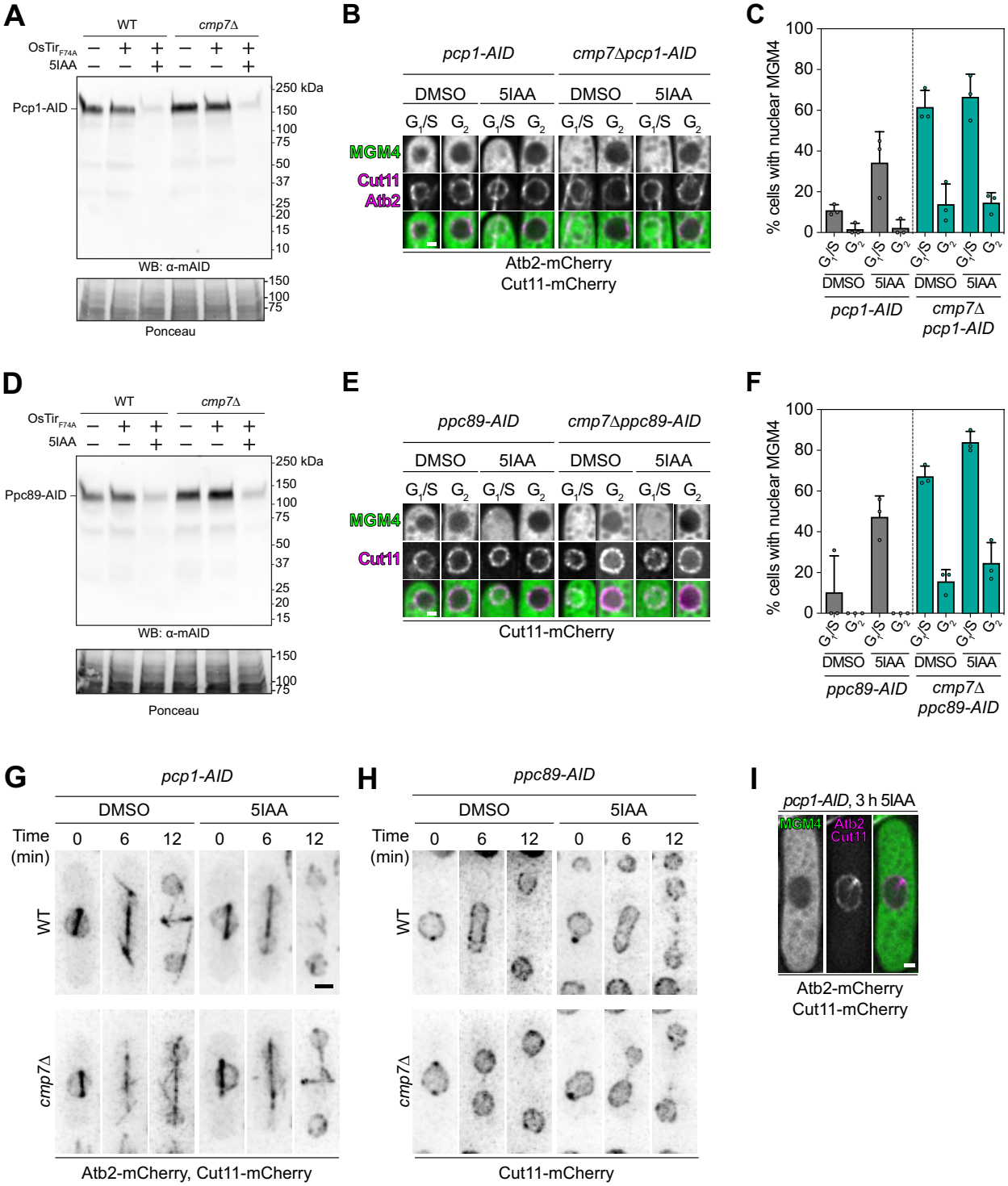

844

Supplementary Figure S5. Conditional degradation of Pcp1 and Ppc89 impairs nucleocytoplasmic compartmentalization without impacting mitosis progression.

Figure legend continued next page.

845

Supplementary Figure S5. Conditional degradation of Pcp1 and Ppc89 impairs nucleocytoplasmic compartmentalization without impacting mitosis progression.

A: Western blot (WB) of Pcp1-AID levels (detected with an α-AID antibody) in total protein extracts from cells expressing OsTir1$_{F74A}$ and treated with 5IAA as indicated. Ponceau stain is shown at bottom to assess relative total protein loads. (-)OsTir1$_{F74A}$ (MKSP4112); (+)OsTir1$_{F74A}$ (MKSP4113); (-)OsTir1$_{F74A}$, *cmp7*Δ (MKSP4114); (+)OsTir1$_{F74A}$, *cmp7*Δ (MKSP4115).

B: Fluorescence micrographs of representative nuclei are shown arranged vertically with MGM4 (green) at top, Cut11-mCherry (magenta) and mCherry-Atb2 (magenta) in middle, and merge at bottom in either *pcp1-AID* (MKSP3773) or *cmp7*Δ*pcp1-AID* (MKSP3775) strains expressing OsTir1$_{F74A}$. Cells were treated with DMSO or 5IAA as indicated. Scale bar, 1 μm.

C: Plot of the percentage of *pcp1-AID* (gray bars, MKSP3773) or *cmp7*Δ*pcp1-AID* (teal bars, MKSP3775) MGM4-expressing cells with N/C fluorescence ratios greater than 0.75 reflecting a loss of nuclear integrity. Points are the mean from each biological replicate, while bars and error bars represent total mean and standard deviation, respectively. Points represent average of at least 18 nuclei/cell cycle phase/strain/replicate, N = 649 nuclei.

D: Western blot (WB) of Ppc89-AID levels (detected with an α-AID antibody) in total protein extracts from cells expressing OsTir1$_{F74A}$ and treated with 5IAA as indicated. Ponceau stain is shown at bottom to assess relative total protein loads. (-)OsTir1$_{F74A}$ (MKSP4175); (+)OsTir1$_{F74A}$ (MKSP4136); (-)OsTir1$_{F74A}$, *cmp7*Δ (MKSP4176); (+)OsTir1$_{F74A}$, *cmp7*Δ (MKSP4135).

E: Fluorescence micrographs of representative nuclei are shown arranged vertically with MGM4 (green) at top, Cut11-mCherry (magenta) and mCherry-Atb2 (magenta) in middle, and merge at bottom in either *ppc89-AID* (MKSP4136) or *cmp7*Δ*ppc89-AID* (MKSP4135) strains expressing OsTir1$_{F74A}$. Cells were treated with DMSO or 5IAA as indicated. Scale bar, 1 μm.

F: Plot of the percentage of *ppc89-AID* (gray bars, MKSP4136) or *cmp7*Δ*ppc89-AID* (teal bars, MKSP4135) MGM4-expressing cells with N/C fluorescence ratios greater than 0.75 reflecting a loss of nuclear integrity. Points are the mean from each biological replicate, while bars and error bars represent total mean and standard deviation, respectively. Points represent average of at least 11 nuclei/cell cycle phase/strain/replicate, N = 504 nuclei.

G: Time-lapse fluorescence microscopy of Atb2-mCherry and Cut11-mCherry in a mitotic *pcp1-AID* (MKSP3773) or *cmp7*Δ*pcp1-AID* cell (MKSP3775) expressing OsTir1$_{F74A}$. Imaging was begun after 1 h treatment with either DMSO or 5IAA as indicated. Scale bar, 1 μm.

H: Time-lapse fluorescence microscopy of Cut11-mCherry in a mitotic *ppc89-AID* (MKSP4136) or *cmp7*Δ*ppc89-AID* cell (MKSP4135) expressing OsTir1$_{F74A}$. Imaging was begun after 1 h treatment with either DMSO or 5IAA as indicated. Scale bar, 1 μm.

I: Fluorescence micrographs of a *pcp1-AID* cell (MKSP3773) expressing OsTir1$_{F74A}$ containing a monopolar spindle arranged horizontally with MGM4 (green) at left, Cut11-mCherry (magenta) and mCherry-Atb2 (magenta) in middle, and merge on right 3 h after treatment with 5IAA. Scale bar, 1 μm.

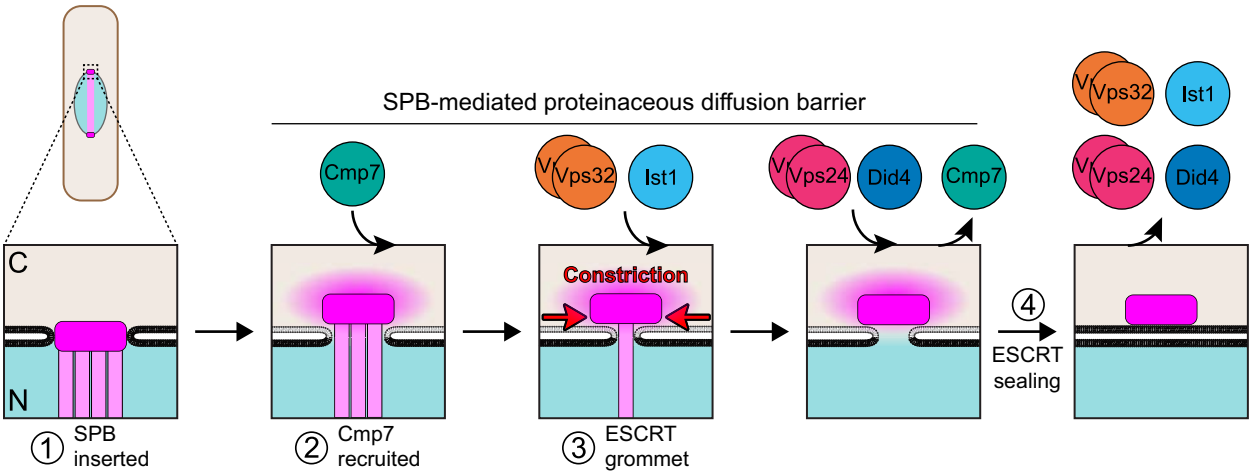

846

Supplementary Figure S6. An ESCRT grommet and SPB-dependent diffusion barrier maintain nuclear integrity

A model of NE sealing and maintenance of mitotic nuclear integrity by the ESCRT machinery and the SPB. (1) In early mitosis, the SPB is inserted into the NE. (2) Once the SPB is extruded to the cytosol, Cmp7 is recruited by Heh1/Lem2 (not shown). Concurrently, the SPB contributes to the formation of a proteinaceous diffusion barrier sensitive to 2.5% 1,6-HD to prevent free diffusion through the unsealed NE. (3) A second wave of ESCRT recruitment comprising Vps32 and Ist1 occurs in late anaphase B, which generates a "grommet" that restricts the size of the NE hole and supports the SPB-dependent diffusion barrier. (4) Finally, in the G_1/S of the following cell cycle, the third wave of ESCRTs, Did4 and Vps24, is recruited, displacing Cmp7 and sealing the NE.

847 **MOVIES**

Movie 1. CLEM and ET of a WT cell in early anaphase B. Electron tomogram of an early anaphase B cell (MKSP3180) with segmentation. NE, blue; SPB, dark orange; microtubules, yellow. Scale bar, 100 nm.

Movie 2. CLEM and ET of a WT cell in late anaphase B. Electron tomogram of a late anaphase B cell (MKSP3180) with segmentation. NE, blue; SPB, dark orange; microtubules, yellow. Annotations at end of movie show NPC and SPB extrusion hole. Scale bar, 100 nm.

Movie 3. CLEM and ET of a *cmp7*Δ cell in early anaphase B. Electron tomogram of an early anaphase B cell (MKSP3243) with segmentation. NE, blue; SPB, dark orange; microtubules, yellow. Scale bar, 100 nm.

Movie 4. CLEM and ET of a *cmp7*Δ cell in late anaphase B. Electron tomogram of a late anaphase B cell (MKSP3243) with segmentation. NE, blue; SPB, dark orange; microtubules, yellow. Scale bar, 100 nm.

848

849 **SUPPLEMENTARY TABLES**

Supplementary Table 1. GFP-tagging of key ESCRT machinery. ESCRT protein in *S. pombe* is shown on left. Orthologs in *S. cerevisiae* and *H. sapiens* are shown in center. Tagging approach to ensure function is shown on right.

Supplementary Table 2. List of *S. pombe* strains used in this study.

Supplementary Table 3. List of plasmids used in this study.

850 **REFERENCES**

851 Adell, M.A.Y., Migliano, S.M., Upadhyayula, S., Bykov, Y.S., Sprenger, S., Pakdel, M., Vogel, G.F., Jih, G.,
852 Skillern, W., Behrouzi, R., et al. (2017). Recruitment dynamics of ESCRT-III and Vps4 to endosomes and
853 implications for reverse membrane budding. Elife *6*, e31652. 10.7554/eLife.31652.

854 Babst, M., Katzmann, D.J., Estepa-Sabal, E.J., Meerloo, T., and Emr, S.D. (2002). ESCRT-III: an
855 endosome-associated heterooligomeric protein complex required for MVB sorting. Dev Cell *3*, 271-282.
856 10.1016/s1534-5807(02)00220-4.

857 Bahler, J., Wu, J.Q., Longtine, M.S., Shah, N.G., McKenzie, A., 3rd, Steever, A.B., Wach, A., Philippsen,
858 P., and Pringle, J.R. (1998). Heterologous modules for efficient and versatile PCR-based gene targeting in
859 *Schizosaccharomyces pombe*. Yeast *14*, 943-951. 10.1002/(SICI)1097-0061(199807)14:10<943::AID-
860 YEA292>3.0.CO;2-Y.

861 Byers, B., and Goetsch, L. (1975). Behavior of spindles and spindle plaques in the cell cycle and conjugation
862 of *Saccharomyces cerevisiae*. J Bacteriol *124*, 511-523. 10.1128/jb.124.1.511-523.1975.

863 Celetti, G., Paci, G., Caria, J., VanDelinder, V., Bachand, G., and Lemke, E.A. (2020). The liquid state of
864 FG-nucleoporins mimics permeability barrier properties of nuclear pore complexes. The Journal of cell
865 biology *219*. 10.1083/jcb.201907157.

866 Chiu, Y.P., Sun, Y.C., Qiu, D.C., Lin, Y.H., Chen, Y.Q., Kuo, J.C., and Huang, J.R. (2020). Liquid-liquid
867 phase separation and extracellular multivalent interactions in the tale of galectin-3. Nature communications
868 *11*, 1229. 10.1038/s41467-020-15007-3.

869 Coyne, A.N., Baskerville, V., Zaepfel, B.L., Dickson, D.W., Rigo, F., Bennett, F., Lusk, C.P., and Rothstein,
870 J.D. (2021). Nuclear accumulation of CHMP7 initiates nuclear pore complex injury and subsequent TDP-
871 43 dysfunction in sporadic and familial ALS. Sci Transl Med *13*. 10.1126/scitranslmed.abe1923.

872 Davis, M.W., and Jorgensen, E.M. (2022). ApE, A Plasmid Editor: a freely available DNA manipulation and
873 visualization program. Front Bioinform *2*, 818619. 10.3389/fbinf.2022.818619.

874 Denais, C.M., Gilbert, R.M., Isermann, P., McGregor, A.L., te Lindert, M., Weigelin, B., Davidson, P.M.,
875 Friedl, P., Wolf, K., and Lammerding, J. (2016). Nuclear envelope rupture and repair during cancer cell
876 migration. Science *352*, 353-358. 10.1126/science.aad7297.

877 Dey, G., Culley, S., Curran, S., Schmidt, U., Henriques, R., Kukulski, W., and Baum, B. (2020). Closed
878 mitosis requires local disassembly of the nuclear envelope. Nature *585*, 119-123. 10.1038/s41586-020-
879 2648-3.

880 Ding, R., West, R.R., Morphew, D.M., Oakley, B.R., and McIntosh, J.R. (1997). The spindle pole body of
881 *Schizosaccharomyces pombe* enters and leaves the nuclear envelope as the cell cycle proceeds. Molecular
882 biology of the cell *8*, 1461-1479. 10.1091/mbc.8.8.1461.

883 Dultz, E., Wojtynek, M., Medalia, O., and Onischenko, E. (2022). The nuclear pore complex: birth, life, and
884 death of a cellular behemoth. Cells *11*. 10.3390/cells11091456.

885 Feng, Z., Caballe, A., Wainman, A., Johnson, S., Haensele, A.F.M., Cottee, M.A., Conduit, P.T., Lea, S.M.,
886 and Raff, J.W. (2017). Structural basis for mitotic centrosome assembly in flies. Cell *169*, 1078-1089 e1013.
887 10.1016/j.cell.2017.05.030.

888 Flory, M.R., Morphew, M., Joseph, J.D., Means, A.R., and Davis, T.N. (2002). Pcp1p, an Spc110p-related
889 calmodulin target at the centrosome of the fission yeast Schizosaccharomyces pombe. Cell Growth Differ
890 *13*, 47-58.

891 Fong, C.S., Sato, M., and Toda, T. (2010). Fission yeast Pcp1 links polo kinase-mediated mitotic entry to
892 gamma-tubulin-dependent spindle formation. The EMBO journal *29*, 120-130. 10.1038/emboj.2009.331.

893 Frey, S., Richter, R.P., and Görlich, D. (2006). FG-rich repeats of nuclear pore proteins form a three-
894 dimensional meshwork with hydrogel-like properties. Science *314*, 815-817. 10.1126/science.1132516.

895 Gibson, D.G., Young, L., Chuang, R.Y., Venter, J.C., Hutchison, C.A., 3rd, and Smith, H.O. (2009).
896 Enzymatic assembly of DNA molecules up to several hundred kilobases. Nature methods *6*, 343-345.
897 10.1038/nmeth.1318.

898 Gu, M., LaJoie, D., Chen, O.S., von Appen, A., Ladinsky, M.S., Redd, M.J., Nikolova, L., Bjorkman, P.J.,
899 Sundquist, W.I., Ullman, K.S., and Frost, A. (2017). LEM2 recruits CHMP7 for ESCRT-mediated nuclear
900 envelope closure in fission yeast and human cells. Proceedings of the National Academy of Sciences of
901 the United States of America *114*, E2166-E2175. 10.1073/pnas.1613916114.

902 Halfmann, C.T., Sears, R.M., Katiyar, A., Busselman, B.W., Aman, L.K., Zhang, Q., O'Bryan, C.S., Angelini,
903 T.E., Lele, T.P., and Roux, K.J. (2019). Repair of nuclear ruptures requires barrier-to-autointegration factor.
904 The Journal of cell biology *218*, 2136-2149. 10.1083/jcb.201901116.

905 Harris, M.A., Rutherford, K.M., Hayles, J., Lock, A., Bahler, J., Oliver, S.G., Mata, J., and Wood, V. (2022).
906 Fission stories: using PomBase to understand *Schizosaccharomyces pombe* biology. Genetics *220*.
907 10.1093/genetics/iyab222.

908 Henne, W.M., Buchkovich, N.J., Zhao, Y., and Emr, S.D. (2012). The endosomal sorting complex ESCRT-
909 II mediates the assembly and architecture of ESCRT-III helices. Cell *151*, 356-371.
910 10.1016/j.cell.2012.08.039.

911 Hentges, P., Van Driessche, B., Tafforeau, L., Vandenhaute, J., and Carr, A.M. (2005). Three novel
912 antibiotic marker cassettes for gene disruption and marker switching in *Schizosaccharomyces pombe*.
913 Yeast *22*, 1013-1019. 10.1002/yea.1291.

914 Huxley, C., Green, E.D., and Dunham, I. (1990). Rapid assessment of *S. cerevisiae* mating type by PCR.
915 Trends Genet *6*, 236. 10.1016/0168-9525(90)90190-h.

916 Jaspersen, S.L. (2021). Anatomy of the fungal microtubule organizing center, the spindle pole body. Curr
917 Opin Struct Biol *66*, 22-31. 10.1016/j.sbi.2020.09.008.

918 Jia, J., Claude-Taupin, A., Gu, Y., Choi, S.W., Peters, R., Bissa, B., Mudd, M.H., Allers, L., Pallikkuth, S.,
919 Lidke, K.A., et al. (2020). Galectin-3 coordinates a cellular system for lysosomal repair and removal. Dev
920 Cell *52*, 69-87 e68. 10.1016/j.devcel.2019.10.025.

921 Jiang, X., Ho, D.B.T., Mahe, K., Mia, J., Sepulveda, G., Antkowiak, M., Jiang, L., Yamada, S., and Jao, L.E.
922 (2021). Condensation of pericentrin proteins in human cells illuminates phase separation in centrosome
923 assembly. Journal of cell science *134*. 10.1242/jcs.258897.

924 Kanke, M., Nishimura, K., Kanemaki, M., Kakimoto, T., Takahashi, T.S., Nakagawa, T., and Masukata, H.
925 (2011). Auxin-inducible protein depletion system in fission yeast. BMC Cell Biol *12*, 8. 10.1186/1471-2121-
926 12-8.

927 Keeney, J.B., and Boeke, J.D. (1994). Efficient targeted integration at leu1-32 and ura4-294 in
928 *Schizosaccharomyces pombe*. Genetics *136*, 849-856.

929 Kinugasa, Y., Hirano, Y., Sawai, M., Ohno, Y., Shindo, T., Asakawa, H., Chikashige, Y., Shibata, S., Kihara,
930 A., Haraguchi, T., and Hiraoka, Y. (2019). The very-long-chain fatty acid elongase Elo2 rescues lethal
931 defects associated with loss of the nuclear barrier function in fission yeast cells. Journal of cell science *132*,
932 jcs229021. 10.1242/jcs.229021.

933 Kono, Y., Adam, S.A., Sato, Y., Reddy, K.L., Zheng, Y., Medalia, O., Goldman, R.D., Kimura, H., and Shimi,
934 T. (2022). Nucleoplasmic lamin C rapidly accumulates at sites of nuclear envelope rupture with BAF and
935 cGAS. The Journal of cell biology *221*, e202201024. 10.1083/jcb.202201024.

936 Kremer, J.R., Mastronarde, D.N., and McIntosh, J.R. (1996). Computer visualization of three-dimensional
937 image data using IMOD. J Struct Biol *116*, 71-76. 10.1006/jsbi.1996.0013.

938 Kroschwald, S., Maharana, S., and Simon, A. (2017). Hexanediol: a chemical probe to investigate the
939 material properties of membrane-less compartments. Matters *3*. 10.19185/matters.201702000010.

940 Krüger, L.K., Sanchez, J.L., Paoletti, A., and Tran, P.T. (2019). Kinesin-6 regulates cell-size-dependent
941 spindle elongation velocity to keep mitosis duration constant in fission yeast. Elife *8*, e42182.
942 10.7554/eLife.42182.

943 Kukulski, W., Schorb, M., Welsch, S., Picco, A., Kaksonen, M., and Briggs, J.A. (2012). Precise, correlated
944 fluorescence microscopy and electron tomography of lowicryl sections using fluorescent fiducial markers.
945 Methods Cell Biol *111*, 235-257. 10.1016/B978-0-12-416026-2.00013-3.

946 Kume, K., Cantwell, H., Burrell, A., and Nurse, P. (2019). Nuclear membrane protein Lem2 regulates
947 nuclear size through membrane flow. Nature communications *10*, 1871. 10.1038/s41467-019-09623-x.

948 Lawrimore, J., Bloom, K.S., and Salmon, E.D. (2011). Point centromeres contain more than a single
949 centromere-specific Cse4 (CENP-A) nucleosome. The Journal of cell biology *195*, 573-582.
950 10.1083/jcb.201106036.

951 Lee, I.J., Stokasimov, E., Dempsey, N., Varberg, J.M., Jacob, E., Jaspersen, S.L., and Pellman, D. (2020).
952 Factors promoting nuclear envelope assembly independent of the canonical ESCRT pathway. The Journal
953 of cell biology *219*. 10.1083/jcb.201908232.

954 Makarova, M., and Oliferenko, S. (2016). Mixing and matching nuclear envelope remodeling and spindle
955 assembly strategies in the evolution of mitosis. Curr Opin Cell Biol *41*, 43-50. 10.1016/j.ceb.2016.03.016.

956 Mastronarde, D.N. (2005). Automated electron microscope tomography using robust prediction of specimen
957 movements. J Struct Biol *152*, 36-51. 10.1016/j.jsb.2005.07.007.

958 Mastronarde, D.N., and Held, S.R. (2017). Automated tilt series alignment and tomographic reconstruction
959 in IMOD. J Struct Biol *197*, 102-113. 10.1016/j.jsb.2016.07.011.

960 McCullough, J., Clippinger, A.K., Talledge, N., Skowyra, M.L., Saunders, M.G., Naismith, T.V., Colf, L.A.,
961 Afonine, P., Arthur, C., Sundquist, W.I., et al. (2015). Structure and membrane remodeling activity of
962 ESCRT-III helical polymers. Science *350*, 1548-1551. 10.1126/science.aad8305.

963 McCullough, J., Frost, A., and Sundquist, W.I. (2018). Structures, functions, and dynamics of ESCRT-
964 III/Vps4 membrane remodeling and fission complexes. Annu Rev Cell Dev Biol *34*, 85-109.
965 10.1146/annurev-cellbio-100616-060600.

966 McDonald, K. (1999). High-pressure freezing for preservation of high resolution fine structure and
967 antigenicity for immunolabeling. Methods Mol Biol *117*, 77-97. 10.1385/1-59259-201-5:77.

968 Mierzwa, B.E., Chiaruttini, N., Redondo-Morata, L., von Filseck, J.M., Konig, J., Larios, J., Poser, I., Muller-
969 Reichert, T., Scheuring, S., Roux, A., and Gerlich, D.W. (2017). Dynamic subunit turnover in ESCRT-III
970 assemblies is regulated by Vps4 to mediate membrane remodelling during cytokinesis. Nature cell biology
971 *19*, 787-798. 10.1038/ncb3559.

972 Moreno, S., Klar, A., and Nurse, P. (1991). Molecular genetic analysis of fission yeast
973 Schizosaccharomyces pombe. Methods Enzymol *194*, 795-823. 10.1016/0076-6879(91)94059-l.

974 Murray, J.M., Watson, A.T., and Carr, A.M. (2016). Transformation of *Schizosaccharomyces pombe*: lithium
975 acetate/dimethyl sulfoxide procedure. Cold Spring Harbor protocols *2016*, pdb prot090969.
976 10.1101/pdb.prot090969.

977 Nguyen, H.C., Talledge, N., McCullough, J., Sharma, A., Moss, F.R., 3rd, Iwasa, J.H., Vershinin, M.D.,
978 Sundquist, W.I., and Frost, A. (2020). Membrane constriction and thinning by sequential ESCRT-III
979 polymerization. Nat Struct Mol Biol *27*, 392-399. 10.1038/s41594-020-0404-x.

980 O'Toole, E.T., Winey, M., and McIntosh, J.R. (1999). High-voltage electron tomography of spindle pole
981 bodies and early mitotic spindles in the yeast *Saccharomyces cerevisiae*. Molecular biology of the cell *10*,
982 2017-2031. 10.1091/mbc.10.6.2017.

983 Olmos, Y., Hodgson, L., Mantell, J., Verkade, P., and Carlton, J.G. (2015). ESCRT-III controls nuclear
984 envelope reformation. Nature *522*, 236-239. 10.1038/nature14503.

985 Olmos, Y., Perdrix-Rosell, A., and Carlton, J.G. (2016). Membrane binding by CHMP7 coordinates ESCRT-
986 III-dependent nuclear envelope reformation. Current biology : CB *26*, 2635-2641.
987 10.1016/j.cub.2016.07.039.

988 Penfield, L., Shankar, R., Szentgyorgyi, E., Laffitte, A., Mauro, M.S., Audhya, A., Muller-Reichert, T., and
989 Bahmanyar, S. (2020). Regulated lipid synthesis and LEM2/CHMP7 jointly control nuclear envelope
990 closure. The Journal of cell biology *219*. 10.1083/jcb.201908179.

991 Petri, M., Frey, S., Menzel, A., Görlich, D., and Techert, S. (2012). Structural characterization of nanoscale
992 meshworks within a nucleoporin FG hydrogel. Biomacromolecules *13*, 1882-1889. 10.1021/bm300412q.

993 Pfitzner, A.K., Mercier, V., Jiang, X., Moser von Filseck, J., Baum, B., Saric, A., and Roux, A. (2020). An
994 ESCRT-III polymerization sequence drives membrane deformation and fission. Cell *182*, 1140-1155 e1118.
995 10.1016/j.cell.2020.07.021.

996 Pfitzner, A.K., Moser von Filseck, J., and Roux, A. (2021). Principles of membrane remodeling by dynamic
997 ESCRT-III polymers. Trends Cell Biol *31*, 856-868. 10.1016/j.tcb.2021.04.005.

998 Pieper, G.H., Sprenger, S., Teis, D., and Oliferenko, S. (2020). ESCRT-III/Vps4 controls heterochromatin-
999 nuclear envelope attachments. Dev Cell *53*, 27-41 e26. 10.1016/j.devcel.2020.01.028.

1000 Popken, P., Ghavami, A., Onck, P.R., Poolman, B., and Veenhoff, L.M. (2015). Size-dependent leak of
1001 soluble and membrane proteins through the yeast nuclear pore complex. Molecular biology of the cell *26*,
1002 1386-1394. 10.1091/mbc.E14-07-1175.

1003 Raab, M., Gentili, M., de Belly, H., Thiam, H.R., Vargas, P., Jimenez, A.J., Lautenschlaeger, F., Voituriez,
1004 R., Lennon-Dumenil, A.M., Manel, N., and Piel, M. (2016). ESCRT III repairs nuclear envelope ruptures
1005 during cell migration to limit DNA damage and cell death. Science *352*, 359-362. 10.1126/science.aad7611.

1006 Radulovic, M., Schink, K.O., Wenzel, E.M., Nahse, V., Bongiovanni, A., Lafont, F., and Stenmark, H. (2018).
1007 ESCRT-mediated lysosome repair precedes lysophagy and promotes cell survival. The EMBO journal *37*.
1008 10.15252/embj.201899753.

1009 Remec Pavlin, M., and Hurley, J.H. (2020). The ESCRTs - converging on mechanism. Journal of cell
1010 science *133*, jcs240333. 10.1242/jcs.240333.

1011 Ribbeck, K., and Görlich, D. (2002). The permeability barrier of nuclear pore complexes appears to operate
1012 via hydrophobic exclusion. The EMBO journal *21*, 2664-2671. 10.1093/emboj/21.11.2664.

1013 Riquelme Barrientos, E., Otto, T.A., Mouton, S.N., Steen, A., and Veenhoff, L.M. (2023). Specificity and
1014 mechanism of 1,6 hexanediol-induced disruption of nuclear transport. bioRxiv, 2023.2003.2030.534880.
1015 10.1101/2023.03.30.534880.

1016 Rosenberg, J.A., Tomlin, G.C., McDonald, W.H., Snydsman, B.E., Muller, E.G., Yates, J.R., and Gould,
1017 K.L. (2006). Ppc89 links multiple proteins, including the septation initiation network, to the core of the fission
1018 yeast spindle-pole body. Molecular biology of the cell *17*, 3793-3805. 10.1091/mbc.e06-01-0039.

1019 Saksena, S., Wahlman, J., Teis, D., Johnson, A.E., and Emr, S.D. (2009). Functional reconstitution of
1020 ESCRT-III assembly and disassembly. Cell *136*, 97-109. 10.1016/j.cell.2008.11.013.

1021 Samwer, M., Schneider, M.W.G., Hoefler, R., Schmalhorst, P.S., Jude, J.G., Zuber, J., and Gerlich, D.W.
1022 (2017). DNA cross-bridging shapes a single nucleus from a set of mitotic chromosomes. Cell *170*, 956-972
1023 e923. 10.1016/j.cell.2017.07.038.

1024 Schindelin, J., Arganda-Carreras, I., Frise, E., Kaynig, V., Longair, M., Pietzsch, T., Preibisch, S., Rueden,
1025 C., Saalfeld, S., Schmid, B., et al. (2012). Fiji: an open-source platform for biological-image analysis. Nature
1026 methods *9*, 676-682. 10.1038/nmeth.2019.

1027 Shulga, N., and Goldfarb, D.S. (2003). Binding dynamics of structural nucleoporins govern nuclear pore
1028 complex permeability and may mediate channel gating. Molecular and cellular biology *23*, 534-542.
1029 10.1128/MCB.23.2.534-542.2003.

1030 Skibinski, G., Parkinson, N.J., Brown, J.M., Chakrabarti, L., Lloyd, S.L., Hummerich, H., Nielsen, J.E.,
1031 Hodges, J.R., Spillantini, M.G., Thusgaard, T., et al. (2005). Mutations in the endosomal ESCRTIII-complex
1032 subunit CHMP2B in frontotemporal dementia. Nature genetics *37*, 806-808. 10.1038/ng1609.

1033 Skowyra, M.L., Schlesinger, P.H., Naismith, T.V., and Hanson, P.I. (2018). Triggered recruitment of ESCRT
1034 machinery promotes endolysosomal repair. Science *360*, eaar5078. 10.1126/science.aar5078.

1035 Sohrmann, M., Schmidt, S., Hagan, I., and Simanis, V. (1998). Asymmetric segregation on spindle poles
1036 of the *Schizosaccharomyces pombe* septum-inducing protein kinase Cdc7p. Genes & development *12*, 84-
1037 94. 10.1101/gad.12.1.84.

1038 Tamm, T., Grallert, A., Grossman, E.P., Alvarez-Tabares, I., Stevens, F.E., and Hagan, I.M. (2011). Brr6
1039 drives the Schizosaccharomyces pombe spindle pole body nuclear envelope insertion/extrusion cycle. The
1040 Journal of cell biology *195*, 467-484. 10.1083/jcb.201106076.

1041 Teis, D., Saksena, S., and Emr, S.D. (2008). Ordered assembly of the ESCRT-III complex on endosomes
1042 is required to sequester cargo during MVB formation. Dev Cell *15*, 578-589. 10.1016/j.devcel.2008.08.013.

1043 Thaller, D.J., Allegretti, M., Borah, S., Ronchi, P., Beck, M., and Lusk, C.P. (2019). An ESCRT-LEM protein
1044 surveillance system is poised to directly monitor the nuclear envelope and nuclear transport system. Elife
1045 *8*, e45284. 10.7554/eLife.45284.

1046 Thaller, D.J., Tong, D., Marklew, C.J., Ader, N.R., Mannino, P.J., Borah, S., King, M.C., Ciani, B., and Lusk,
1047 C.P. (2021). Direct binding of ESCRT protein Chm7 to phosphatidic acid-rich membranes at nuclear
1048 envelope herniations. The Journal of cell biology *220*. 10.1083/jcb.202004222.

1049 Ungricht, R., and Kutay, U. (2017). Mechanisms and functions of nuclear envelope remodelling. Nature
1050 reviews. Molecular cell biology *18*, 229-245. 10.1038/nrm.2016.153.

1051 Ventimiglia, L.N., Cuesta-Geijo, M.A., Martinelli, N., Caballe, A., Macheboeuf, P., Miguet, N., Parnham,
1052 I.M., Olmos, Y., Carlton, J.G., Weissenhorn, W., and Martin-Serrano, J. (2018). CC2D1B coordinates
1053 ESCRT-III activity during the mitotic reformation of the nuclear envelope. Dev Cell *47*, 547-563 e546.
1054 10.1016/j.devcel.2018.11.012.

1055 Vietri, M., Radulovic, M., and Stenmark, H. (2020). The many functions of ESCRTs. Nature reviews.
1056 Molecular cell biology *21*, 25-42. 10.1038/s41580-019-0177-4.

1057 Vietri, M., Schink, K.O., Campsteijn, C., Wegner, C.S., Schultz, S.W., Christ, L., Thoresen, S.B., Brech, A.,
1058 Raiborg, C., and Stenmark, H. (2015). Spastin and ESCRT-III coordinate mitotic spindle disassembly and
1059 nuclear envelope sealing. Nature *522*, 231-235. 10.1038/nature14408.

1060 von Appen, A., LaJoie, D., Johnson, I.E., Trnka, M.J., Pick, S.M., Burlingame, A.L., Ullman, K.S., and Frost,
1061 A. (2020). LEM2 phase separation promotes ESCRT-mediated nuclear envelope reformation. Nature *582*,
1062 115-118. 10.1038/s41586-020-2232-x.

1063 Wälde, S., and King, M.C. (2014). The KASH protein Kms2 coordinates mitotic remodeling of the spindle
1064 pole body. Journal of cell science *127*, 3625-3640. 10.1242/jcs.154997.

1065 Wallis, S.S., Ventimiglia, L.N., Otigbah, E., Infante, E., Cuesta-Geijo, M.A., Kidiyoor, G.R., Carbajal, M.A.,
1066 Fleck, R.A., Foiani, M., Garcia-Manyes, S., et al. (2021). The ESCRT machinery counteracts Nesprin-2G-
1067 mediated mechanical forces during nuclear envelope repair. Dev Cell *56*, 3192-3202 e3198.
1068 10.1016/j.devcel.2021.10.022.

1069 Webster, B.M., Colombi, P., Jäger, J., and Lusk, C.P. (2014). Surveillance of nuclear pore complex
1070 assembly by ESCRT-III/Vps4. Cell *159*, 388-401. 10.1016/j.cell.2014.09.012.

1071 Webster, B.M., Thaller, D.J., Jäger, J., Ochmann, S.E., Borah, S., and Lusk, C.P. (2016). Chm7 and Heh1
1072 collaborate to link nuclear pore complex quality control with nuclear envelope sealing. The EMBO journal
1073 *35*, 2447-2467. 10.15252/embj.201694574.

1074 West, R.R., Vaisberg, E.V., Ding, R., Nurse, P., and McIntosh, J.R. (1998). cut11(+): A gene required for
1075 cell cycle-dependent spindle pole body anchoring in the nuclear envelope and bipolar spindle formation in
1076 *Schizosaccharomyces pombe*. Molecular biology of the cell *9*, 2839-2855. 10.1091/mbc.9.10.2839.

1077 Wood, V., Gwilliam, R., Rajandream, M.A., Lyne, M., Lyne, R., Stewart, A., Sgouros, J., Peat, N., Hayles,
1078 J., Baker, S., et al. (2002). The genome sequence of *Schizosaccharomyces pombe*. Nature *415*, 871-880.
1079 10.1038/nature724.

1080 Woodruff, J.B., Ferreira Gomes, B., Widlund, P.O., Mahamid, J., Honigmann, A., and Hyman, A.A. (2017).
1081 The centrosome Is a selective condensate that nucleates microtubules by concentrating tubulin. Cell *169*,
1082 1066-1077 e1010. 10.1016/j.cell.2017.05.028.

1083 Zhang, X.R., Zhao, L., Suo, F., Gao, Y., Wu, Q., Qi, X., and Du, L.L. (2022). An improved auxin-inducible
1084 degron system for fission yeast. G3 (Bethesda) *12*, jkab393. 10.1093/g3journal/jkab393.

1085 Zwicker, D., Decker, M., Jaensch, S., Hyman, A.A., and Julicher, F. (2014). Centrosomes are autocatalytic
1086 droplets of pericentriolar material organized by centrioles. Proceedings of the National Academy of
1087 Sciences of the United States of America *111*, E2636-2645. 10.1073/pnas.1404855111.
1088

Supplementary Table S1. GFP-tagging of key ESCRT machinery			
Protein	Orthologs		GFP tagging approach
S. pombe	*S. cerevisiae*	*H. sapiens*	
Cmp7	Chm7	CHMP7	Endogenous, C-terminal 3×HA-mEGFP
Vps32	Snf7	CHMP4A-C	Ectopic in *vps32*Δ, N-terminal 3×HA-mEGFP
Ist1	Ist1	IST1	Endogenous, C-terminal 3×HA-mEGFP
Vps24	Vps24	CHMP3	Ectopic in *vps24*Δ, N-terminal 3×HA-mEGFP
Did4	Vps2	CHMP2A,B	Ectopic in did*4*Δ, N-terminal 3×HA-mEGFP
Did2	Did2	CHMP1A,B	Endogenous, C-terminal 3×HA-mEGFP

Supplementary Table S2. Complete list of *S. pombe* strains used in this study		
Strain (MKSP)	**Genotype**	**Origin**
280	*pcp1::pcp1-15-HA::hygMX6* | *leu1-32* | *ura4-D18* | *h-*	CSF0076 (Fong et al., 2010); gift from Takashi Toda
281	*pcp1::pcp1-18-HA::hygMX6* | *leu1-32* | *ura4-D18* | *h-*	CSF0082 (Fong et al., 2010); gift from Takashi Toda
399	*leu1-32* | *ura4-D18* | *ade6-* | *h+*	Lab stock
1303	*mto1::kanMX6* | *leu1-32* | *ura4-D18* | *ade6-* | *h+*	Frost Lab
1305	*mto2::kanMX6* | *leu1-32* | *ura4-D18* | *ade6-* | *h+*	Frost Lab
1461	*plo1::plo1-24C* | *leu1-32* | *ura4-D18* | *h-*	Constructed in Wälde et al., 1998
1474	*natMX6::nmt81-GFP-Kms2-3'::kanMX6 (kms2 DAmP)* | *aurR-pnda3-mCherry-atb2*| *ade6-M?* | *ura4-D18* | *leu1-32* | *h-*	Constructed in Wälde et al., 2014
1697	*cut11::cut11-GFP:ura4+* | *aurR-pnda3-mCherry-atb2* | *ade6-M?* | *leu1?* | *ura4-D18* | *h-*	Constructed in this work, derived from CSF0511 (Fong et al., 2010) and PN#3779 (West et al., 1998)
3180	*cdc7::cdc7-GFP:kanMX6* | *pcp1::pcp1-mCherry:kanMX6* | *leu1-32* | *ura4-D18*	This work
3186	*fta3::fta3-mEGFP::kanMX6* | *leu1-32* | *ura4-D18* | *ade6-M210*	MSA007 (Pollard Lab)
3243	*cmp7::hygMX6* | *cdc7::cdc7-GFP:kanMX6* | *pcp1::pcp1-mCherry:kanMX6* | *leu1-32* | *ura4-D18*	This work
3259	*cmp7::cmp7-3×HA-mEGFP:kanMX6* | *heh1::natMX6* | *aurR-pnda3-mCherry-atb2* | *leu1-32* | *ura4-D18*	Constructed in this work, derived from CSF0511 (Fong et al., 2010)
3275	*cmp7::cmp7-3×HA-mEGFP:kanMX6* | *heh2::hygMX6* | *aurR-pnda3-mCherry-atb2* | *leu1-32?* | *ura4-D18?*	Constructed in this work, derived from CSF0511 (Fong et al., 2010)
3334	*leu1::*P_{did4}*-mEGFP-3×HA-did4-*T_{did4} | *did4::hygMX6* | *sad1::sad1-mCherry:kanMX6* | *aurR-pnda-mCherry-atb2* | *ura4-D18* | *h-*	Constructed in this work, derived from CSF0511 (Fong et al., 2010)
3340	*cmp7::natMX6* | *aurR-pnda3-mCherry-atb2* | *leu1-32* | *h+*	Constructed in this work, derived from CSF0511 (Fong et al., 2010)
3342	*did2::did2-3×HA-mEGFP:kanMX6* | *pcp1::pcp1-mCherry:natMX6* | *aurR-pnda3-mCherry-atb2* | *leu1-32* | *ura4-D18* | *h-*	Constructed in this work, derived from CSF0511 (Fong et al., 2010)
3345	*leu1::P41nmt1-MBP-yeGFP-4×MBP-*T_{cyc1} | ura4-D18 | h+	This work
3352	*leu1::*P_{vps24}*-mEGFP-3×HA-vps24-*T_{vps24} | *vps24::hygMX6* | *pcp1::pcp1-mCherry:kanMX6* | *aurR-pnda-mCherry-atb2* | *ura4-D18* | *h-*	Constructed in this work, derived from CSF0511 (Fong et al., 2010)
3353	*leu1::*P_{vps32}*-mEGFP-3×HA-vps32-*T_{vps32} | *vps32::hygMX6* | *pcp1::pcp1-mCherry:natMX6* | *aurR-pnda-mCherry-atb2* | *ura4-D18* | *h-*	Constructed in this work, derived from CSF0511 (Fong et al., 2010)
3354	*leu1::*P_{vps32}*-mEGFP-3×HA-vps32-*T_{vps32} | *vps32::hygMX6* | *cmp7::natMX6* | *pcp1::pcp1-mCherry:kanMX6* | *aurR-pnda-mCherry-atb2* | *ura4-D18* | *h?*	Constructed in this work, derived from CSF0511 (Fong et al., 2010)
3355	*leu1::*P_{vps24}*-mEGFP-3×HA-vps24-*T_{vps24} | *vps24::hygMX6* | *cmp7::natMX6* | *pcp1::pcp1-mCherry:kanMX6* | *aurR-pnda-mCherry-atb2* | *ura4-D18*	Constructed in this work, derived from CSF0511 (Fong et al., 2010)
3363	*cmp7::cmp7-3×HA-mEGFP:kanMX6* | *pcp1::pcp1-mCherry:natMX6* | *aurR-pnda3-mCherry-atb2* | *leu1-32* | *ura4-D18* | *h-*	Constructed in this work, derived from CSF0511 (Fong et al., 2010)
3365	*ist1::ist1-3×HA-mEGFP:kanMX6* | *sad1::sad1-mCherry:natMX6* | *aurR-pnda3-mCherry-atb2* | *leu1-32* | *ura4-D18* | *h-*	Constructed in this work, derived from CSF0511 (Fong et al., 2010)
3366	*leu1::*P_{did4}*-mEGFP-3×HA-did4-*T_{did4} | *did4::hygMX6* | *cmp7::natMX6* | *sad1::sad1-mCherry:kanMX6* | *aurR-pnda-mCherry-atb2* | *ura4-D18*	Constructed in this work, derived from CSF0511 (Fong et al., 2010)
3381	*cmp7::cmp7-3×HA-mEGFP:kanMX6* | *did4::hygMX6* | *pcp1::pcp1-mCherry:natMX6* | *aurR-pnda3-mCherry-atb2* | *leu1-32* | *ura4-D18*	Constructed in this work, derived from CSF0511 (Fong et al., 2010)
3385	*cmp7::cmp7-3×HA-mEGFP:kanMX6* | *vps32::hygMX6* | *aurR-pnda3-mCherry-atb2* | *leu1-32* | *ura4-D18*	Constructed in this work, derived from CSF0511 (Fong et al., 2010)
3387	*cmp7::cmp7-3×HA-mEGFP:kanMX6* | *vps24::hygMX6* | *aurR-pnda3-mCherry-atb2* | *leu1-32* | *ura4-D18*	Constructed in this work, derived from CSF0511 (Fong et al., 2010)
3420	*cmp7::natMX6* | *pcp1::pcp1-15-HA::hygMX6* | *leu1-32* | *ura4-D18* | *h+*	Constructed in this work, derived from CSF0511 (Fong et al., 2010)
3425	*cmp7::kanMX6* | *pcp1::pcp1-18-HA::hygMX6* | *leu1-32* | *ura4-D18* | *h+*	Constructed in this work, derived from CSF0511 (Fong et al., 2010)
3429	*cmp7::cmp7-3×HA-mEGFP:kanMX6* | *ist1::hygMX6* | *pcp1::pcp1-mCherry:natMX6* | *aurR-pnda3-mCherry-atb2* | *leu1-32* | *ura4-D18*	Constructed in this work, derived from CSF0511 (Fong et al., 2010)
3447	*ist1::ist1-3×HA-mEGFP:kanMX6* |*cmp7::hygMX6* | *sad1::sad1-mCherry:natMX6* | *aurR-pnda3-mCherry-atb2* | *leu1-32* | *ura4-D18* | *h?*	Constructed in this work, derived from CSF0511 (Fong et al., 2010)
3449	*leu1::*P_{vps32}*-mEGFP-3×HA-vps32-*T_{vps32} | *vps32::hygMX6* | *ist1::kanMX6* | *pcp1::pcp1-mCherry:natMX6* | *aurR-pnda-mCherry-atb2* | *ura4-D18*	Constructed in this work, derived from CSF0511 (Fong et al., 2010)

Supplementary Table S2. Complete list of *S. pombe* strains used in this study		
Strain (MKSP)	**Genotype**	**Origin**
3461	*brr6::brr6.ts8:ura4 | ura4-D18*	IH3620 (Hagan Lab)
3468	*sad1::sad1-1 (A323V) | leu1-32*	YGRC FY10254
3469	*cut11::cut11-1 | leu1-32*	YGRC FY11773
3475	*alp6::alp6-719 | leu1-32*	YGRC FY33773
3476	*mzt1::mzt1-T27W:hygMX6 | leu1-32 | ura4-D18 | lys1-131 | his7?*	YGRC FY33777
3488	*leu1::P41$_{nmt1}$-MBP-yeGFP-4×MBP-T$_{cyc1}$ | aurR-pnda-mCherry-atb2 | ura4-D18 | h+*	This work
3496	*ist1::ist1-3×HA-mEGFP:kanMX6 |did4::hygMX6 | sad1::sad1-mCherry:natMX6 | aurR-pnda3-mCherry-atb2 | leu1-32 | ura4-D18*	Constructed in this work, derived from CSF0511 (Fong et al., 2010)
3504	*ist1::ist1-3×HA-mEGFP:kanMX6 | vps32::hygMX6 | sad1::sad1-mCherry:natMX6 | aurR-pnda3-mCherry-atb2 | leu1-32 | ura4-D18*	Constructed in this work, derived from CSF0511 (Fong et al., 2010)
3511	*leu1::P$_{vps24}$-mEGFP-3×HA-vps24-T$_{vps24}$ | vps24::hygMX6 | did4:kanMX6 | pcp1::pcp1-mCherry:kanMX6 | aurR-pnda-mCherry-atb2 | ura4-D18 | h-*	Constructed in this work, derived from CSF0511 (Fong et al., 2010)
3517	*cmp7::cmp7-XTEN16-3×sAID:kanMX6 | ura4::Padh1-OsTIR1-F74A | leu1-32 | ade6?*	Constructed in this work, derived from DY48569 (Zhang et al., 2022)
3521	*cmp7::cmp7-3×HA-mEGFP:kanMX6 | ist1::ist1-3×HA-mCherry:kanMX6 | leu1-32 | ura4-D18 | h-*	This work
3528	*leu1::P41$_{nmt1}$-MBP-yeGFP-2×MBP-T$_{cyc1}$ | cmp7::hygMX6 | brr6::brr6.ts8:ura4 | aurR-pnda-mCherry-atb2 | ura4-D18 | h+*	Constructed in this work, derived from MKSP3461
3535	*leu1::P41$_{nmt1}$-MBP-yeGFP-4×MBP | cmp7::hygMX6 | aurR-pnda-mCherry-atb2 | ura4-D18 | ade6-M210 | h-*	This work
3544	*ist1::ist1-3×HA-mEGFP:kanMX6 | vps24::kanMX6 | sad1::sad1-mCherry:natMX6 | aurR-pnda3-mCherry-atb2 | leu1-32 | ura4-D18*	Constructed in this work, derived from CSF0511 (Fong et al., 2010)
3557	*leu1::P41$_{nmt1}$-MBP-yeGFP-4×MBP-T$_{cyc1}$ | vps32::hygMX6 | aurR-pnda-mCherry-atb2 | ura4-D18 | h+*	This work
3559	*leu1::P41$_{nmt1}$-MBP-yeGFP-4×MBP-T$_{cyc1}$ | ist1::kanMX6 | aurR-pnda-mCherry-atb2 | ura4-D18 | h+*	This work
3586	*leu1::P41$_{nmt1}$-MBP-yeGFP-4×MBP-T$_{cyc1}$ | did4::hygMX6 | aurR-pnda-mCherry-atb2 | ura4-D18 | h+*	This work
3592	*leu1::P41$_{nmt1}$-MBP-yeGFP-4×MBP-T$_{cyc1}$ | vps24::kanMX6 | aurR-pnda-mCherry-atb2 | ura4-D18 | h+*	This work
3593	*leu1::P41$_{nmt1}$-MBP-yeGFP-4×MBP-T$_{cyc1}$ | did2::hygMX6 | aurR-pnda-mCherry-atb2 | ura4-D18 | h+*	This work
3625	*ist1::ist1-3×HA-mEGFP:kanMX6 | cmp7-XTEN16-3×sAID::kanMX6 | ura4+::P$_{adh1}$-OsTIR1$_{F74A}$ | sad1::sad1-mCherry:natMX6 | aurR-pnda3-mCherry-atb2 | leu1-32 | ade6-M216*	Constructed in this work, derived from CSF0511 (Fong et al., 2010) and DY48569 (Zhang et al., 2022)
3668	*leu1::P$_{did4}$-mEGFP-3×HA-did4-T$_{did4}$ | did4::hygMX6 | ist1::natMX6 | sad1::sad1-mCherry:kanMX6 | aurR-pnda-mCherry-atb2 | ura4-D18*	Constructed in this work, derived from CSF0511 (Fong et al., 2010)
3669	*leu1::P$_{vps24}$-mEGFP-3×HA-vps24-T$_{vps24}$ | vps24::hygMX6 | ist1::natMX6 | pcp1::pcp1-mCherry:natMX6 | aurR-pnda-mCherry-atb2 | ura4-D18*	Constructed in this work, derived from CSF0511 (Fong et al., 2010)
3683	*cmp7::hygMX6 | natMX6::nmt81-GFP-Kms2-3'::kanMX6 (kms2 DAmP) | aurR-pnda3-mCherry-atb2 | ade6-M? | ura4-D18 | leu1-32 | h-*	This work
3699	*leu1::P41$_{nmt1}$-MBP-yeGFP-4×MBP-T$_{cyc1}$ | cmp7::cmp7-XTEN16-3×sAID:kanMX6 | ura4::P$_{adh1}$-OsTIR1$_{F74A}$ | cut11::cut11-mCherry:natMX6 | h+*	Constructed in this work, derived from DY48569 (Zhang et al., 2022)
3773	*leu1::P41$_{nmt1}$-MBP-yeGFP-4×MBP-T$_{cyc1}$ | pcp1::pcp1-XTEN16-3×sAID:kanMX6 | ura4::P$_{adh1}$-OsTIR1$_{F74A}$ | cut11::cut11-mCherry:natMX6 | aurR-pnda3-mCherry-atb2 | h-*	Constructed in this work, derived from DY48569 (Zhang et al., 2022)
3775	*leu1::P41$_{nmt1}$-MBP-yeGFP-4×MBP-T$_{cyc1}$ | cmp7::hygMX6 | pcp1::pcp1-XTEN16-3×sAID:kanMX6 | ura4::P$_{adh1}$-OsTIR1$_{F74A}$ | cut11::cut11-mCherry:natMX6 | aurR-pnda3-mCherry-atb2 | h-*	Constructed in this work, derived from DY48569 (Zhang et al., 2022)
3811	*leu1::P41$_{nmt1}$-MBP-yeGFP-4×MBP-T$_{cyc1}$ | cmp7::natMX6 | pcp1::pcp1-15-HA::hygMX6 | cut11::cut11-mCherry:natMX6 | ura4-D18 | h+*	Constructed in this work, derived from CSF0511 (Fong et al., 2010)
3812	*leu1::P41$_{nmt1}$-MBP-yeGFP-4×MBP-T$_{cyc1}$ | pcp1::pcp1-15-HA::hygMX6 | cut11::cut11-mCherry:natMX6 | ura4-D18 | h+*	Constructed in this work, derived from CSF0511 (Fong et al., 2010)
3960	*leu1::P41$_{nmt1}$-MBP-yeGFP-2×MBP-T$_{cyc1}$ | cut11::cut11-mCherry:natMX6 | aurR-pnda-mCherry-atb2 | ura4-D18 | h+*	This work
4027	*mto1::kanMX6 | cmp7::hygMX6 | aurR-pnda3-mCherry-atb2 | leu1-32 | ura4-D18 | ade6?*	Constructed in this work, derived from MKSP1303
4031	*alp6::alp6-719 | cmp7::HygR | leu1-32*	Constructed in this work, derived from MKSP3475

Supplementary Table S2. Complete list of *S. pombe* strains used in this study		
Strain (MKSP)	**Genotype**	**Origin**
4033	*sad1::sad1-1 | cmp7::HygR | leu1-32*	Constructed in this work, derived from MKSP3468
4040	*cut11::cut11-1 | cmp7::HygR | leu1-32*	Constructed in this work, derived from MKSP3469
4045	*mzt1::mzt1-T27W:hygMX6 | cmp7::HygR | leu1-32 | lys1? | his7?*	Constructed in this work, derived from MKSP3476
4048	*plo1::plo1-24C | cmp7::HygR | leu1-32 | ura4-D18*	Constructed in this work, derived from MKSP1461
4060	*cdc11::cdc11-123 | leu1-32 | h-*	YGRC FY8347
4061	*cam1::cam1-116F:ura4+ | leu1-32 | ade6-M216 | ura4-D18 | h-*	YGRC FY13263
4062	*gtb1::gtb1-93 | leu1 | h-*	YGRC FY1441
4063	*alp14::ura4+ | leu1-32 | ura4-D18*	YGRC FY17702
4065	*sid4::sid4-SA1 | leu1-32 | ura4-D18 | ade6-M21?*	YGRC FY29119
4067	*alp4::alp4-1891 | leu1-32 | ura4-D18| his2*	YGRC FY33772
4106	*cdc7::cdc7-GFP::kanMX6 | pcp1::pcp1-15-HA::hygMX6 | cmp7::natMX6 | leu1-32 | ura4-D18 |*	This work
4107	*cdc7::cdc7-GFP::kanMX6 | pcp1::pcp1-15-HA::hygMX6 | leu1-32 | ura4-D18 |*	This work
4112	*leu1::P41$_{nmt1}$-MBP-yeGFP-4×MBP-T$_{cyc1}$ | pcp1::pcp1-XTEN16-3×sAID:kanMX6 | cut11::cut11-mCherry:natMX6*	Constructed in this work, derived from DY48569 (Zhang et al., 2022)
4113	*leu1::P41$_{nmt1}$-MBP-yeGFP-4×MBP-T$_{cyc1}$ | pcp1::pcp1-XTEN16-3×sAID:kanMX6 | ura4::P$_{adh1}$-OsTIR1$_{F74A}$ | cut11::cut11-mCherry:natMX6*	Constructed in this work, derived from DY48569 (Zhang et al., 2022)
4114	*leu1::P41$_{nmt1}$-MBP-yeGFP-4×MBP-T$_{cyc1}$ | pcp1::pcp1-XTEN16-3×sAID:kanMX6 | cmp7::HygR | cut11::cut11-mCherry:natMX6*	Constructed in this work, derived from DY48569 (Zhang et al., 2022)
4115	*leu1::P41$_{nmt1}$-MBP-yeGFP-4×MBP-T$_{cyc1}$ | pcp1::pcp1-XTEN16-3×sAID:kanMX6 | cmp7::HygR | ura4::P$_{adh1}$-OsTIR1$_{F74A}$ | cut11::cut11-mCherry:natMX6*	Constructed in this work, derived from DY48569 (Zhang et al., 2022)
4135	*leu1::P41$_{nmt1}$-MBP-yeGFP-4×MBP-T$_{cyc1}$ | ppc89::ppc89-XTEN16-3×sAID:kanMX6 | cmp7::HygR | ura4::P$_{adh1}$-OsTIR1$_{F74A}$ | cut11::cut11-mCherry:natMX6*	This work
4136	*leu1::P41$_{nmt1}$-MBP-yeGFP-4×MBP-T$_{cyc1}$ | ppc89::ppc89-XTEN16-3×sAID:kanMX6 | ura4::P$_{adh1}$-OsTIR1$_{F74A}$ | cut11::cut11-mCherry:natMX6*	This work
4151	*mto2::kanMX6 | cmp7::hygMX6 | aurR-pnda3-mCherry-atb2 | leu1-32 | ura4-D18 | ade6?*	Constructed in this work, derived from MKSP1305
4163	*alp4::alp4-1891 | cmp7::hygR | leu1-32 | ura4-D18| his2*	Constructed in this work, derived from MKSP4067
4165	*alp14::ura4+ | cmp7::hygR | leu1-32 | ura4-D18*	Constructed in this work, derived from MKSP4063
4167	*cam1::cam1-116F:ura4+ | cmp7::hygR | leu1-32 | ade6-M216 | ura4-D18*	Constructed in this work, derived from MKSP4061
4169	*cdc11::cdc11-123 | cmp7::hygR | leu1-32*	Constructed in this work, derived from MKSP4060
4171	*sid4::sid4-SA1 | cmp7::hygR | leu1-32 | ura4-D18 | ade6-M21?*	Constructed in this work, derived from MKSP4065
4174	*gtb1::gtb1-93 | cmp7::hygR | leu1 | h-*	Constructed in this work, derived from MKSP4062
4175	*leu1::P41$_{nmt1}$-MBP-yeGFP-4×MBP-T$_{cyc1}$ | ppc89::ppc89-XTEN16-3×sAID:kanMX6 | cut11::cut11-mCherry:natMX6*	This work
4176	*leu1::P41$_{nmt1}$-MBP-yeGFP-4×MBP-T$_{cyc1}$ | ppc89::ppc89-XTEN16-3×sAID:kanMX6 | cmp7::HygR | cut11::cut11-mCherry:natMX6*	This work

Supplementary Table S3. Complete list of plasmids used in this study

Identifier	Name/Description	Usage	Origin
pNA8	pFA6a-3×HA-mEGFP-KanMX6	Template for PCR based chromosomal integration of 3×HA-mEGFP ORF	This study; Addgene 87023
pNA22	pJK148-P_{vps32}-mEGFP-3×HA-vps32-T_{vps32}	Linearized with NruI and transformed into MKSP975	This study, Gibson assembly
pNA23	pJK148-P_{vps24}-mEGFP-3×HA-vps24-T_{vps24}	Linearized with NruI and transformed into MKSP975	This study, Gibson assembly
pNA33	pFA6a-hygMX6	Integration cassette amplification hygMX6 template	Hentges et al., 2005
pNA34	pFA6a-natMX6	Integration cassette amplification natMX6 template	Hentges et al., 2005
pNA35	pFA6a-kanMX6	Template for PCR based chromosomal integration of kanMX6 ORF	Wach et al., 1997; Addgene 39296
pNA45	pJK148-P_{did4}-mEGFP-3×HA-did4-T_{did4}	Linearized with NruI and transformed into MKSP975	This study, Gibson assembly
pNA47	pFA6a-mCherry-KanMX6	Template for PCR based chromosomal integration of mCherry ORF	EUROSCARF
pNA48	pFA6a-mCherry-NatMX6	Template for PCR based chromosomal integration of mCherry ORF	EUROSCARF
pNA50	pFA6a-3×HA-mCherry-NatMX6	Template for PCR based chromosomal integration of 3×HA-mCherry ORF	This study
pNA55	pDB4581_pFA6a-3×sAID-KanMX6	Template for PCR based chromosomal integration of 3×sAID ORF	Zhang et al., 2022; Addgene 171124
pNA63	pJK148-P41$_{nmt1}$-MBP-yeGFP-4×MBP-T_{cyc1}	Linearized with NruI and transformed into MKSP399	Popken et al., 2015 and this study, restriction digest cloning